

# A plug-and-play approach with fast uncertainty quantification for weak lensing mass mapping

H. Leterme<sup>1,2,\*</sup>, A. Tersenov<sup>2,3,\*\*</sup>, J. Fadili<sup>1</sup>, and J.-L. Starck<sup>2,3</sup>

<sup>1</sup> Université Caen Normandie, ENSICAEN, CNRS, Normandie Univ, GREYC UMR 6072, F-14000 Caen, France

<sup>2</sup> Université Paris-Saclay, Université Paris Cité, CEA, CNRS, AIM, 91191, Gif-sur-Yvette, France

<sup>3</sup> Institutes of Computer Science and Astrophysics, Foundation for Research and Technology Hellas (FORTH), Heraklion, Greece

## ABSTRACT

*Context.* Upcoming stage-IV surveys such as Euclid and Rubin will deliver vast amounts of high-precision data, opening new opportunities to constrain cosmological models with unprecedented accuracy. A key step in this process is the reconstruction of the dark matter distribution from noisy weak lensing shear measurements.

*Aims.* Current deep learning-based mass mapping methods achieve high reconstruction accuracy, but either require retraining a model for each new observed sky region—limiting practicality—or rely on slow MCMC sampling. Efficient exploitation of future survey data therefore calls for a new method that is accurate, flexible, and fast at inference. In addition, uncertainty quantification with coverage guarantees is essential for reliable cosmological parameter estimation.

*Methods.* We introduce PnPMass, a plug-and-play approach for weak lensing mass mapping. The algorithm produces point estimates by alternating between a gradient descent step with a carefully chosen data fidelity term, and a denoising step implemented with a single deep learning model trained on simulated data corrupted by Gaussian white noise. We also propose a fast, sampling-free uncertainty quantification scheme based on moment networks, with calibrated error bars obtained through conformal prediction to ensure coverage guarantees. Finally, we benchmark PnPMass against both model-driven and data-driven mass mapping techniques.

*Results.* PnPMass achieves performance close to that of state-of-the-art deep-learning methods while offering fast inference—converging in just a few iterations—and requiring only a single training phase, independently of the noise covariance of the observations. It therefore combines flexibility, efficiency, and reconstruction accuracy, while delivering tighter error bars than existing approaches, making it well suited for upcoming weak lensing surveys.

**Key words.** cosmology: observations – methods: statistical – gravitational lensing: weak

## 1. Introduction

In the coming years, next-generation observational instruments such as the Euclid space telescope and the Vera C. Rubin Observatory will deliver galaxy catalogs with unprecedented precision and sky coverage. These surveys are expected to enhance our understanding of large-scale structures in the Universe and refine existing models of its formation.

A central task in analyzing data from such surveys is mass mapping through weak gravitational lensing. The aim is to reconstruct the distribution of dark matter from noisy shear measurements, which capture the distortion of galaxy shapes caused by inhomogeneous mass distribution along the line of sight (Kaiser & Squires 1993). The resulting mass maps are then used to constrain the plausible ranges of cosmological parameters. Accurate mass mapping is crucial for optimizing cosmological inference—recent work by Tersenov et al. (2025) showed that replacing the classical Kaiser-Squires method (Kaiser & Squires 1993) with a more advanced algorithm such as MCALens (Starck et al. 2021) can significantly improve the figure of merit (FoM) in realistic weak lensing pipelines. Moreover, it is essential to rigorously quantify uncertainty, as errors in mass reconstruction can propagate to the estimation of cosmological parameters, potentially amplifying discrepancies.

In recent years, deep learning-based approaches have achieved state-of-the-art reconstruction accuracy in weak lensing mass mapping. Two notable examples are DeepMass (Jeffrey et al. 2020), which directly predicts a point estimate from a noisy shear map, and DeepPosterior (Remy et al. 2023), a Bayesian method that samples from the posterior distribution of the mass map. Despite their performances, both methods face limitations that are incompatible with upcoming stage-IV surveys such as Euclid and Rubin, where vast amounts of data are set to be delivered. DeepMass offers fast inference, as a single forward pass through the network suffices to produce a point estimate from an initial, computationally inexpensive estimate derived from a noisy observation. However, as an end-to-end method, the network is sensitive to factors like varying noise levels and masks, and must therefore be retrained for each new observation. DeepPosterior, by contrast, is more flexible and does not require retraining, but inference is computationally expensive since multiple samples must be drawn to obtain a single point estimate.

In this paper, we introduce PnPMass, a novel deep learning-based method for weak lensing mass mapping that, like DeepMass, generates accurate point estimates without posterior sampling and, like DeepPosterior, does not require retraining for each new observation. Our approach builds on the plug-and-play (PnP) framework (Venkatakrisnan et al. 2013), which enables efficient reconstruction by integrating deep priors into physical models. PnP methods have become widespread in computational imaging and physical modeling (Kamilov et al. 2023), and have

\* hubert.leterme@cea.fr

\*\* atersenov@physics.uoc.gr

Table 1: Qualitative comparison of mass mapping methods.

	Accurate	Flexible	Fast rec.	Fast UQ
DeepMass	✓	✗*	✓	✓
DeepPosterior	✓	✓	✗	✗
<b>PnPMass (ours)</b>	✓	✓	✓	✓

**Notes.** \*Requires specific retraining for each new observation.

seen growing theoretical support in recent years (Ryu et al. 2019; Terris et al. 2020; Hurault et al. 2022; Ebner & Haltmeier 2024), including convergence guarantees to a fixed point under appropriate conditions. Our key insight is to show that, with appropriate algorithmic design—particularly regarding the data-fidelity term—it is possible to train a denoiser on white Gaussian noise with standard deviation randomly drawn from a given interval, independently of the noise characteristics of the actual observation. This allows for high flexibility across datasets and survey conditions while maintaining fast and accurate reconstructions.

Additionally, we propose an uncertainty quantification (UQ) method for PnPMass that does not rely on sampling. Specifically, we adapt the moment network approach by Jeffrey & Wandelt (2020), originally developed for end-to-end methods like DeepMass, to our PnP framework. To obtain statistically calibrated uncertainty estimates, we further apply Conformalized Quantile Regression (CQR) (Romano et al. 2019) to derive per-pixel error bars with provable coverage guarantees.

Our experiments, conducted on the  $\kappa$ TNG simulated dataset (Osato et al. 2021), demonstrate that PnPMass achieves competitive reconstruction accuracy while remaining flexible—the model is trained once for all, unlike DeepMass—and requiring only a few iterations at inference—significantly fewer than those needed by DeepPosterior for sampling. Furthermore, our UQ method, which requires only one additional iteration to compute per-pixel intervals, produces smaller error bars than DeepMass. A qualitative comparison of PnPMass with DeepMass and DeepPosterior is provided in Table 1.

This paper is organized as follows. In Sect. 2, we review the mass mapping problem and existing data-driven reconstruction methods. In Sect. 3, we present the PnPMass framework. In Sect. 4, we introduce our UQ pipeline, including the method based on moment networks in Sect. 4.1, and CQR-based calibration in Sect. 4.2. Sections 5 and 6 detail our experimental setup and results. We conclude and discuss future directions in Sect. 7.

## 2. Background on weak lensing mass mapping

In this paper, deterministic vectors are denoted with bold lowercase Greek or Latin letters (*e.g.*  $\boldsymbol{\kappa}$ ), while random vectors are represented with bold sans-serif capital letters (*e.g.*  $\mathbf{K}$ ). Deterministic matrices are indicated by standard bold capital letters (*e.g.*  $\mathbf{A}$ ). Furthermore, indexing is done using brackets ( $\boldsymbol{\kappa}[k]$ ,  $\mathbf{K}[k]$ , or  $\mathbf{A}[k, l]$ ).

### 2.1. The mass mapping problem

This section provides a brief overview of the weak lensing mass mapping problem, for which a comprehensive review has been proposed by Kilbinger (2015). The objective is to recover a convergence map  $\boldsymbol{\kappa} \in \mathbb{R}^{K^2}$ , which causes isotropic dilations of background galaxies, from a shear map  $\boldsymbol{\gamma} \in \mathbb{C}^{K^2}$ , which induces anisotropic stretching. Both fields are discretized over a square grid of size  $K \times K$ , with  $K \in \mathbb{N}$ , and represented as flattened

one-dimensional vectors. In the weak lensing regime, the convergence is proportional to the projected mass along the line of sight between the background galaxies and the observer (Kaiser & Squires 1993). Reconstructing the convergence field is thus equivalent to estimating the projected mass distribution.

In practice, only variations in  $\boldsymbol{\kappa}$  around its mean value can be recovered, due to mass-sheet degeneracy. Similarly, only the variations in  $\boldsymbol{\gamma}$  around its mean value contribute to the reconstruction. We therefore assume, without loss of generality, that both  $\boldsymbol{\kappa}$  and  $\boldsymbol{\gamma}$  are zero-centered. Under this assumption, a first-order relationship between shear and convergence can be expressed as:

$$\boldsymbol{\gamma} = \mathbf{A}\boldsymbol{\kappa}, \quad (1)$$

where  $\mathbf{A} \in \mathbb{C}^{K^2 \times K^2}$  is a linear operator defined as:

$$\mathbf{A} := \mathbf{F}^* \mathbf{P} \mathbf{F}, \quad (2)$$

where  $\mathbf{F}$  and its adjoint (Hermitian / conjugate transpose)  $\mathbf{F}^* \in \mathbb{C}^{K^2 \times K^2}$  represent the two-dimensional discrete Fourier and inverse Fourier transforms, respectively. Moreover,  $\mathbf{P} \in \mathbb{C}^{K^2 \times K^2}$  is a diagonal matrix satisfying  $\mathbf{P}[0, 0] = 0$ , and for all  $(k_1, k_2) \in \{0, \dots, K-1\}^2 \setminus \{(0, 0)\}$ ,

$$\mathbf{P}[Kk_1 + k_2, Kk_1 + k_2] := \frac{(k_1 + ik_2)^2}{k_1^2 + k_2^2}. \quad (3)$$

Due to  $\mathbf{P}$  being zero at the zero frequency, the operator  $\mathbf{A}$  is not invertible. Its kernel is the subspace of constant vectors, whereas its image is the subspace of zero-mean vectors. The pseudo-inverse of  $\mathbf{A}$  is equal to its adjoint  $\mathbf{A}^*$ , which shares the same kernel and image. Therefore, the convergence map can be recovered via:

$$\boldsymbol{\kappa} = \mathbf{A}^* \boldsymbol{\gamma}, \quad (4)$$

yielding an exact reconstruction when both  $\boldsymbol{\gamma}$  and  $\boldsymbol{\kappa}$  are restricted to the subspace of zero-mean vectors.

A direct observation of the shear, however, is impossible in practice. Instead, a noisy estimator can be obtained by binning a galaxy catalog at the desired resolution and averaging the corresponding galaxy ellipticities within each pixel. Then, (1) becomes:

$$\boldsymbol{\gamma} = \mathbf{M}\mathbf{A}\boldsymbol{\kappa} + \mathbf{n}, \quad (5)$$

where  $\mathbf{M} \in \{0, 1\}^{K^2 \times K^2}$  is a diagonal matrix encoding the observational mask (*e.g.*, survey boundaries or contamination from bright stars in the foreground), and  $\mathbf{n} \in \mathbb{C}^{K^2}$  is a realization of proper complex Gaussian noise  $\mathbf{N}$  with zero-mean and diagonal covariance matrix  $\boldsymbol{\Sigma} \in \mathbb{R}^{K^2 \times K^2}$ . For any pixel  $k \in \{1, \dots, K^2\}$  where  $\mathbf{M}[k, k] = 1$ , the variance is given by:

$$\boldsymbol{\Sigma}[k, k] = \sigma_{\text{ell}}^2 / N_k, \quad (6)$$

where  $\sigma_{\text{ell}}^2 > 0$  is the variance of intrinsic ellipticities, and  $N_k$  is the number of galaxies observed in pixel  $k$ .

For pixels  $k \in \{1, \dots, K^2\}$  such that  $\mathbf{M}[k, k] = 0$  (*i.e.*, within masked regions), we adopt a strategy similar to that proposed by Starck et al. (2021); Remy et al. (2023): the noise variance  $\boldsymbol{\Sigma}[k, k]$  is artificially set to a very high value in order to reduce the signal-to-noise ratio (S/R) to near zero. Then, (5) can be approximated by:

$$\boldsymbol{\gamma} = \mathbf{A}\boldsymbol{\kappa} + \mathbf{n}. \quad (7)$$

In the remaining of the paper, pixels outside and within the mask are referred to as active pixels and masked pixels, respectively.

## 2.2. Overview of mass mapping methods

### 2.2.1. Classical approaches

The most simple method to the mass mapping problem has been proposed by [Kaiser & Squires \(1993\)](#), and is later referred to as the Kaiser-Squires (KS) solution. It consists in applying (4) to the noisy shear map  $\boldsymbol{\gamma}$ , followed by Gaussian smoothing to reduce the noise. More recent approaches have proposed to adopt a variational framework by solving minimization problems of the form

$$\hat{\boldsymbol{\kappa}} \in \operatorname{argmin}_{\boldsymbol{\kappa}' \in \mathbb{R}^{K^2}} f_{\boldsymbol{\gamma}}(\mathbf{A}\boldsymbol{\kappa}') + g(\boldsymbol{\kappa}'), \quad (8)$$

where  $f_{\boldsymbol{\gamma}}(\mathbf{A}\boldsymbol{\kappa}')$  represents a data fidelity term measuring the resemblance between  $\boldsymbol{\gamma}$  and  $\mathbf{A}\boldsymbol{\kappa}'$ , while  $g$  denotes a handcrafted regularization function penalizing unexpected solutions. Notable examples include iterative Wiener filtering ([Bobin et al. 2012](#)), a forward-backward splitting algorithm with  $\ell^2$  regularization corresponding to a Gaussian prior with predefined power spectrum; the GLIMPSE2D algorithm ([Lanusse et al. 2016](#)), which enforces sparsity in a wavelet dictionary; and the MCALens algorithm ([Starck et al. 2021](#)), which models the solution as a combination of a Gaussian and a sparse component in a wavelet dictionary.

### 2.2.2. Data-driven approaches

Deep learning models have demonstrated significantly improved reconstruction accuracy over classical approaches by learning the distribution of convergence maps from large datasets of simulations. From a Bayesian perspective, where the convergence map  $\boldsymbol{\kappa}$  is viewed as the realization of a random vector  $\mathbf{K}$  with an unknown distribution, the inverse problem (7) becomes:

$$\boldsymbol{\Gamma} = \mathbf{A}\mathbf{K} + \mathbf{N}, \quad (9)$$

where  $\boldsymbol{\Gamma}$  denotes the random vector from which  $\boldsymbol{\gamma}$  is drawn.

Among deep learning-based approaches, DeepMass ([Jeffrey et al. 2020](#)) takes the noisy shear map  $\boldsymbol{\gamma}$  as input, computes a naive estimate such as the KS or iterative Wiener solution, passes it through a deep neural network (typically, a UNet), and outputs an enhanced reconstruction  $\hat{\boldsymbol{\kappa}}_{\text{dm}}$ . The model is trained on simulated pairs of convergence maps and their corresponding noisy shear maps,  $(\boldsymbol{\gamma}_i, \boldsymbol{\kappa}_i)_{i=1}^n$ , following the forward model (7).

While DeepMass achieves high reconstruction accuracy, it suffers from a major limitation: it requires retraining for each new observation  $\boldsymbol{\gamma}$ , as the noise covariance  $\boldsymbol{\Sigma}$  depends on the galaxy number density in each pixel. As a result, the training data must be adapted accordingly, reducing the method’s flexibility.

Alternatively, DeepPosterior ([Remy et al. 2023](#)) generates samples from the posterior  $p_{\mathbf{K}|\boldsymbol{\Gamma}=\boldsymbol{\gamma}}(\cdot)$  by using a Markov Chain Monte-Carlo (MCMC) algorithm. In this approach, the prior  $p_{\mathbf{K}}(\cdot)$  is implicitly learned via neural score matching. Then, averaging over the samples yields a point estimate  $\hat{\boldsymbol{\kappa}}_{\text{dp}}$ . This method directly allows for UQ by computing sample statistics. In contrast to the previous approach, DeepPosterior only needs to be trained once, independently of the noise properties. However, inference is slow, as it requires many samples to produce a single estimate.

Other methods have been proposed, with similar limitations. [Shirasaki et al. \(2019, 2021\)](#); [Aoyama et al. \(2025\)](#) introduced mass mapping techniques based on conditional generative adversarial networks (GANs) or diffusion models. Recently, [Whitney](#)

[et al. \(2025\)](#) developed a fast sampling method based on conditional Wasserstein GANs, significantly reducing generation time per sample compared to DeepPosterior. Despite their state-of-the-art performances, the above methods suffer from the same limitations as DeepMass: the training phase is specific to a given observation and therefore lack flexibility. More precisely, given a newly-observed sky area, or another galaxy survey, these models must be re-trained relatively to the new configuration—with a specific mask  $\mathbf{M}$  and per-pixel noise level  $\boldsymbol{\Sigma}$ . Our approach specifically addresses this issue.

## 3. Proposed approach based on plug-and-play

In this section, we introduce PnPMass, a PnP-based algorithm specifically tailored for the mass mapping problem. We cast the problem into a real-valued formulation, where we define:

$$\tilde{\boldsymbol{\gamma}} := \begin{pmatrix} \operatorname{Re} \boldsymbol{\gamma} \\ \operatorname{Im} \boldsymbol{\gamma} \end{pmatrix} \in \mathbb{R}^{2K^2}, \quad \tilde{\boldsymbol{n}} := \begin{pmatrix} \operatorname{Re} \boldsymbol{n} \\ \operatorname{Im} \boldsymbol{n} \end{pmatrix} \in \mathbb{R}^{2K^2}, \quad (10)$$

$$\tilde{\mathbf{A}} := \begin{pmatrix} \operatorname{Re} \mathbf{A} \\ \operatorname{Im} \mathbf{A} \end{pmatrix} \in \mathbb{R}^{2K^2 \times K^2}, \quad \tilde{\boldsymbol{\Sigma}} := \frac{1}{2} \begin{pmatrix} \boldsymbol{\Sigma} & \mathbf{0} \\ \mathbf{0} & \boldsymbol{\Sigma} \end{pmatrix} \in \mathbb{R}^{2K^2 \times 2K^2}. \quad (11)$$

Then, (7) becomes

$$\tilde{\boldsymbol{\gamma}} = \tilde{\mathbf{A}}\boldsymbol{\kappa} + \tilde{\boldsymbol{n}}, \quad (12)$$

where the noise  $\tilde{\boldsymbol{n}}$  is a realization of  $\tilde{\mathbf{N}} \sim \mathcal{N}(\mathbf{0}, \tilde{\boldsymbol{\Sigma}})$ .

In Sect. 3.1, we introduce a fixed-point iteration composed of a “forward” step, involving a linear operator  $\tilde{\mathbf{B}}$  and a step-size  $\tau > 0$ , followed by a “backward” step using a deep denoiser  $\mathcal{D}_{\hat{\theta}}$ . Sect. 3.2 establishes properties on  $\mathcal{D}_{\hat{\theta}}$  that enable accurate recovery of the convergence map  $\boldsymbol{\kappa}$  from the noisy shear input  $\boldsymbol{\gamma}$ . In Sect. 3.3, we show that a suitable choice of  $\tilde{\mathbf{B}}$  allows the denoiser to be trained on white Gaussian noise, independently of the noise covariance matrix  $\tilde{\boldsymbol{\Sigma}}$ . Sect. 3.4 then derives bounds on  $\tau$  to guarantee convergence to a fixed point. Additionally, Sect. 3.5 details properties required for the denoiser, including fixed-point conditions, and noise-level awareness. Finally, in Sect. 3.6, we present a variant of PnPMass that incorporates prior knowledge of the Gaussian structure of convergence maps, outside peak regions dominated by large matter aggregates.

### 3.1. Fixed-point iteration

Given an observation  $\tilde{\boldsymbol{\gamma}} \in \mathbb{R}^{2K^2}$  and a step-size  $\tau > 0$ , we introduce a “forward” operator  $\mathcal{F}_{\tilde{\boldsymbol{\gamma}}}(\cdot, \tau) : \mathbb{R}^{K^2} \rightarrow \mathbb{R}^{K^2}$ , defined, for any input  $\boldsymbol{\kappa}'$ , by:

$$\mathcal{F}_{\tilde{\boldsymbol{\gamma}}}(\boldsymbol{\kappa}', \tau) := \boldsymbol{\kappa}' + \tau \tilde{\mathbf{B}}(\tilde{\boldsymbol{\gamma}} - \tilde{\mathbf{A}}\boldsymbol{\kappa}'), \quad (13)$$

where  $\tilde{\mathbf{B}} \in \mathbb{R}^{K^2 \times 2K^2}$  denotes a linear operator to be defined. We also consider a deep learning-based denoiser  $\mathcal{D}_{\hat{\theta}} : \mathbb{R}^{K^2} \rightarrow \mathbb{R}^{K^2}$  with trained parameters  $\hat{\theta}$ . The PnP method, inspired by standard operator splitting methods in optimization theory for solving inverse problems—see ([Starck et al. 2015](#)) and Appendix F—consists in iterating the operator  $\mathcal{H}_{\tilde{\boldsymbol{\gamma}}}(\cdot, \tau)$  taken as the composition of the forward operator and the trained denoiser:

$$\mathcal{H}_{\tilde{\boldsymbol{\gamma}}}(\cdot, \tau) := \mathcal{D}_{\hat{\theta}} \circ \mathcal{F}_{\tilde{\boldsymbol{\gamma}}}(\cdot, \tau). \quad (14)$$

Towards studying the properties of this operator, we state our main assumptions:

- (H.1)  $\mathcal{D}_\theta : (\ker \tilde{\mathbf{B}}\tilde{\mathbf{A}})^\perp \rightarrow (\ker \tilde{\mathbf{B}}\tilde{\mathbf{A}})^\perp$ ;
- (H.2)  $\mathcal{D}_\theta$  is non-expansive on  $(\ker \tilde{\mathbf{B}}\tilde{\mathbf{A}})^\perp$ , i.e.,  $\beta$ -Lipschitz continuous on  $(\ker \tilde{\mathbf{B}}\tilde{\mathbf{A}})^\perp$  with  $\beta \leq 1$ ;
- (H.3)  $\tilde{\mathbf{B}}\tilde{\mathbf{A}}$  is symmetric positive semidefinite;
- (H.4)  $\text{ran } \tilde{\mathbf{B}} \subset (\ker \tilde{\mathbf{B}}\tilde{\mathbf{A}})^\perp$ ;
- (H.5) Let  $\lambda_{\min}$  and  $\lambda_{\max} = \|\tilde{\mathbf{B}}\tilde{\mathbf{A}}\|$  denote, respectively, the minimum and maximum nonzero eigenvalues of  $\tilde{\mathbf{B}}\tilde{\mathbf{A}}$ . We also introduce:

$$\rho^* := \frac{\lambda_{\max} - \lambda_{\min}}{\lambda_{\max} + \lambda_{\min}}. \quad (15)$$

For fixed  $\rho \in [\rho^*, 1[$ , the step-size  $\tau$  satisfies

$$\frac{1 - \rho}{\lambda_{\min}} \leq \tau \leq \frac{1 + \rho}{\lambda_{\max}}. \quad (16)$$

Under the above assumptions, the operator  $\mathcal{H}_{\tilde{\gamma}}(\cdot, \tau)$  enjoys the following properties.

**Proposition 1.** *Under assumptions (H.1)–(H.5), the operator  $\mathcal{H}_{\tilde{\gamma}}(\cdot, \tau)$  admits a unique fixed point  $\hat{\kappa} \in (\ker \tilde{\mathbf{B}}\tilde{\mathbf{A}})^\perp$ . Moreover, the sequence of iterates  $(\kappa^{(k)})_{k \in \mathbb{N}}$  defined by*

$$\kappa^{(k+1)} = \mathcal{H}_{\tilde{\gamma}}(\kappa^{(k)}, \tau), \quad (17)$$

starting at  $\kappa^{(0)} \in (\ker \tilde{\mathbf{B}}\tilde{\mathbf{A}})^\perp$ , converges linearly to  $\hat{\kappa}$  with convergence rate  $\rho$ .

*Proof.* See Appendix A.

### 3.2. Which noise to train the denoiser ?

Under the above assumptions,  $\hat{\kappa}$  obeys the fixed-point equation

$$\hat{\kappa} = \mathcal{D}_\theta(\hat{\kappa} + \tau\tilde{\mathbf{B}}(\tilde{\gamma} - \tilde{\mathbf{A}}\hat{\kappa})). \quad (18)$$

Assessing whether the fixed point  $\hat{\kappa}$  lies sufficiently close to the true convergence map  $\kappa$  is a challenging question that falls beyond the scope of this paper. A mathematical framework is nevertheless sketched in Appendix B, thereby constraining the noise level at which the denoiser  $\mathcal{D}_\theta$  must be trained.

Our intuition can be summarized as follows. Assuming the residual  $\hat{r} := \hat{\kappa} - \kappa$  is small enough, by applying the forward step to the fixed point  $\hat{\kappa}$ , we get the following approximation:

$$\hat{\kappa}_0 := \mathcal{F}_{\tilde{\gamma}}(\hat{\kappa}, \tau) = \kappa + \hat{r} + \tau\tilde{\mathbf{B}}(-\tilde{\mathbf{A}}\hat{r} + \tilde{n}) \quad (19)$$

$$\approx \kappa + \tau\tilde{\mathbf{B}}\tilde{n}. \quad (20)$$

Therefore, applying the operator  $\mathcal{H}_{\tilde{\gamma}}$  introduced in (14) to the fixed point  $\hat{\kappa}$  yields

$$\hat{\kappa} = \mathcal{D}_\theta(\hat{\kappa}_0) \approx \mathcal{D}_\theta(\kappa + \tau\tilde{\mathbf{B}}\tilde{n}). \quad (21)$$

Thus,  $\mathcal{D}_\theta$  acts as a denoiser on the true convergence map  $\kappa$  corrupted by a Gaussian noise  $\mathbf{n}_0 := \tau\tilde{\mathbf{B}}\tilde{n} \in \mathbb{R}^{K^2}$ , which is an outcome of

$$\mathbf{N}_0 := \tau\tilde{\mathbf{B}}\tilde{\mathbf{N}} \sim \mathcal{N}(\mathbf{0}, \Sigma_0), \quad \text{with } \Sigma_0 := \tau^2\tilde{\mathbf{B}}\tilde{\Sigma}\tilde{\mathbf{B}}^\top. \quad (22)$$

In practice, we train the denoiser by minimizing the empirical quadratic risk,

$$\hat{\theta} \in \underset{\theta}{\text{argmin}} \frac{1}{n} \sum_{i=1}^n \left\| \mathcal{D}_\theta(\kappa_i + \mathbf{n}_{0,i}) - \kappa_i \right\|^2, \quad (23)$$

using a dataset of  $n$  training samples, where the ground truth convergence maps  $\kappa_i$  are generated from simulations based on the  $\Lambda$ CDM model, and the noisy inputs are computed from  $\kappa_i$  by adding noise  $\mathbf{n}_{0,i}$  drawn according to (22).

### 3.3. Choice of operator $\tilde{\mathbf{B}}$

One of the main objectives of this paper is to implement a mass mapping method whose training phase is *independent* of the training noise covariance matrix  $\tilde{\Sigma}$ . Clearly, given our discussion in Sect. 3.2, the covariance matrix  $\Sigma_0$  in (22) must be independent of  $\tilde{\Sigma}$ . To this end, we use the degree of freedom offered by the choice of  $\tilde{\mathbf{B}}$ . More precisely, we propose to make the following choice:

$$\tilde{\mathbf{B}} := \tilde{\mathbf{A}}^\top \tilde{\Sigma}^{-1/2}, \quad (24)$$

in which case (22) and (13) become:

$$\Sigma_0 = \tau^2 \tilde{\mathbf{A}}^\top \tilde{\mathbf{A}} \quad \text{and} \quad \mathcal{F}_{\tilde{\gamma}}(\kappa', \tau) := \kappa' + \tau \tilde{\mathbf{A}}^\top \tilde{\Sigma}^{-1/2} (\tilde{\gamma} - \tilde{\mathbf{A}}\kappa'). \quad (25)$$

Beware here that strictly speaking,  $\Sigma_0$  is not a covariance matrix as it is only semidefinite positive with  $\ker \Sigma_0 = \ker \mathbf{A}$ , the subspace of constant vectors. But this is fine as we are only interested in random perturbations along  $(\ker \tilde{\mathbf{B}}\tilde{\mathbf{A}})^\perp = (\ker \mathbf{A})^\perp$ , where  $\Sigma_0$  is symmetric positive definite.

In Appendix C, we show that with the choice (24),  $\tilde{\mathbf{B}}\tilde{\mathbf{A}} = \tilde{\mathbf{A}}^\top \tilde{\Sigma}^{-1/2} \tilde{\mathbf{A}}$  verifies assumptions (H.3) and (H.4). In fact, we even have the equality  $\text{ran } \tilde{\mathbf{B}} = (\ker \tilde{\mathbf{B}}\tilde{\mathbf{A}})^\perp$ .

By closely inspecting (25), one sees that the residual  $\tilde{\gamma} - \tilde{\mathbf{A}}\kappa'$  is multiplied by  $\tilde{\Sigma}^{-1/2}$ , which corresponds to a noise-whitening step. This is in a stark contrast with the choice  $\tilde{\mathbf{B}} := \tilde{\mathbf{A}}^\top \tilde{\Sigma}^{-1}$ , which yields  $\mathcal{F}_{\tilde{\gamma}}(\kappa', \tau) := \kappa' + \tau \tilde{\mathbf{A}}^\top \tilde{\Sigma}^{-1} (\tilde{\gamma} - \tilde{\mathbf{A}}\kappa')$ . This alternative choice is the one dictated by the standard variational (or Bayesian MAP) perspective with a data fidelity  $\frac{1}{2} \|\tilde{\Sigma}^{-1/2} (\tilde{\gamma} - \tilde{\mathbf{A}}\kappa')\|^2$  as negative log-likelihood, whose gradient is  $\tilde{\mathbf{A}}^\top \tilde{\Sigma}^{-1} (\tilde{\gamma} - \tilde{\mathbf{A}}\kappa')$ . This clearly shows that the widely-adopted optimization or Bayesian perspective on PnP is not necessarily the most appropriate one and may even be misleading in the PnP context—see also the discussion in Appendix F. The fixed-point perspective, on the other hand, offers more insight and flexibility.

In Appendix D, we show that

$$\tilde{\mathbf{A}}^\top \tilde{\mathbf{A}} = \mathbf{I} - \frac{1}{K^2}, \quad (26)$$

(the constant  $1/K^2$  is subtracted from all matrix elements). In practice, the image size  $K$  is sufficiently large to neglect the non-diagonal elements. Therefore, from (25) and (26), it is valid to take the approximation

$$\Sigma_0 \approx \tau^2 \mathbf{I}. \quad (27)$$

In turn, the denoiser  $\mathcal{D}_\theta$  is trained on zero-mean white Gaussian noise with a standard deviation equal to the step-size  $\tau$ . In Sect. 3.4, we discuss how to select an appropriate range for  $\tau$ .

### 3.4. Step-size selection

As discussed in Sect. 3.1, existence and uniqueness of a fixed point as well as convergence of the PnP iteration (17) to this fixed point require  $\tau$  to satisfy (H.5). Substituting the expression for  $\tilde{\mathbf{B}}$  from (24), condition (16) specializes to

$$\frac{1 - \rho}{\lambda_{\min}} \leq \tau \leq \frac{1 + \rho}{\lambda_{\max}}, \quad \text{where } \lambda_{\max} = \|\tilde{\mathbf{A}}^\top \tilde{\Sigma}^{-1/2} \tilde{\mathbf{A}}\|. \quad (28)$$

It is well known that  $\lambda_{\max}$  can be accurately computed via the power iteration method. In Appendix E, we will also discuss how the power iteration can be used to efficiently compute  $\lambda_{\min}$ .

One can also get a simple estimate of the upper-bound for  $\tau$  via an upper bound of  $\lambda_{\max}$ . Indeed, observe that

$$\begin{aligned} \|\tilde{\mathbf{A}}^\top \tilde{\Sigma}^{-1/2} \tilde{\mathbf{A}}\| &\leq \|\tilde{\mathbf{A}}^\top \tilde{\mathbf{A}}\| \|\tilde{\Sigma}^{-1/2}\| \\ &\leq \|\tilde{\Sigma}^{-1/2}\| = 1/\min_k \tilde{\sigma}_k, \end{aligned}$$

where we have used (26) and  $\tilde{\sigma}_k := \tilde{\Sigma}[k, k]^{1/2}$  denotes the noise standard deviation at pixel  $k$ . Therefore,

$$\tau \leq (1 + \rho) \min_k \tilde{\sigma}_k, \quad (29)$$

is a sufficient condition for the right hand side of (28) to hold. Thus, the choice of the largest step-size is essentially governed by the smallest noise level in the input shear map—that is, the pixel with the largest number of observed galaxies.

### 3.5. Denoiser training

#### 3.5.1. Ensuring convergence to a fixed point

The denoiser ought to comply with (H.1) and (H.2) for Proposition 1 to hold. As discussed in Sect. 3.3 (see also Appendix C), with the choice of  $\tilde{\mathbf{B}}$  given in (24), one has

$$(\ker \tilde{\mathbf{B}} \tilde{\mathbf{A}})^\perp := \ker(\tilde{\mathbf{A}})^\perp, \quad (30)$$

that is, the subspace of zero-mean convergence maps. In turn, (H.1) tells us that the denoiser must not introduce any bias, *i.e.* the denoised version of a zero-mean map must also be zero-mean. This is a natural and expected property. It is consistent with the mass-sheet degeneracy property discussed in Sect. 2.1 and can be enforced by explicitly appending a mean-centering layer at the output of the denoiser.

Regarding the non-expansiveness assumption (H.2), it can be encouraged during training by introducing a regularization term that controls the spectral norm of the denoiser’s Jacobian (Pesquet et al. 2021). However, this strategy is computationally very expensive, and we simply chose to ignore this constraint in practice. A theoretical understanding of the training dynamics, including a potential implicit bias towards non-expansive denoisers, would be valuable. This avenue is beyond the scope of this work and is left for future research.

#### 3.5.2. Noise-level-aware denoiser

According to the discussions in Sects. 3.2, 3.3 and 3.4, the denoiser  $\mathcal{D}_\theta$  is trained by solving (23), where  $\mathbf{n}_{0,i}$  are sampled from a zero-mean white Gaussian distribution with variance  $\tau^2$ . The bound (29) shows that the noise level  $\tau$  used for training depends on the noise covariance matrix  $\tilde{\Sigma}$  of the mass mapping problem. Therefore, at this stage, the training phase remains dependent on  $\tilde{\Sigma}$ . However, this dependence now reduces to a single scalar  $\tau$ , whereas the full (diagonal) covariance matrix was required for training DeepMass.

We aim to push this one step forward by making the training phase completely independent of the covariance matrix. One simple strategy would be to select a small value for  $\tau$ , to cover a broad range of survey conditions. However, as our experiments confirm, the choice of  $\tau$  strongly affects reconstruction quality.

We therefore adopt a more flexible approach, in which the model is enabled to adapt to different noise conditions during inference. To this end, the network is trained on a dataset  $(\kappa_{0,i}, \kappa_i)_{i=1}^n$ , where each input  $\kappa_{0,i}$  is obtained by corrupting the ground truth  $\kappa_i$  by noise  $\mathbf{n}_{0,i}$  drawn from  $\mathcal{N}(\mathbf{0}, \sigma_i^2)$ , with  $\sigma_i$  being

randomly picked among a wide range of noise levels. For higher reconstruction accuracy, we use a noise-level-aware model, following an approach initially proposed by Zhang et al. (2022). In this context, the denoiser network takes the noise standard deviation  $\sigma$  as an additional entry, *i.e.*  $\mathcal{D}_\theta(\kappa', \sigma)$ , where  $\sigma > 0$  denotes the noise standard deviation at which the model is expected to operate.

During inference with PnPMass, according to (27), the intermediate outputs are propagated through the network with noise standard deviation  $\tau$ . Then, the fixed-point iteration introduced in (14) now reads

$$\mathcal{H}_{\tilde{\gamma}}(\cdot, \tau) := \mathcal{D}_\theta(\cdot, \tau) \circ \mathcal{F}_{\tilde{\gamma}}(\cdot, \tau), \quad (31)$$

where now, both the forward and denoising steps depend on the step-size  $\tau$ . This is again reminiscent of the forward-backward splitting (FBS) algorithm as discussed in Appendix F.

#### 3.5.3. Training on multiple cosmologies

Generating training data via simulation requires selecting a set of cosmological parameters, which implicitly shapes the prior distribution from which convergence map samples are drawn. If the chosen parameters diverge significantly from the true, unknown cosmology that one wants to infer, the trained denoiser may struggle to generalize and thus fail to produce accurate reconstructions. One way to overcome this is to generate training data across a distribution of plausible cosmologies, enhancing the network’s robustness to distributional shifts.

### 3.6. PnPMass on non-Gaussian residuals

In the spirit of DeepMass (Jeffrey et al. 2020), the PnPMass algorithm can be enhanced by considering a priori knowledge about the underlying physics and data structure. For this, we use a hypothesis made by Starck et al. (2021) for MCALens: convergence maps can be seen as the superposition of a Gaussian field and a non-Gaussian one (hereafter referred to as a residual field):

$$\kappa = \kappa^g + \kappa^{\text{ng}}, \quad (32)$$

where  $\kappa^g$ , the Gaussian component, can be estimated from the noisy shear map  $\gamma$  using an iterative Wiener filtering method (see Sect. 2.2.1), assuming the power spectrum  $\mathbf{P}_g$  is known, coined  $\mathcal{W}_{\mathbf{P}_g}$ ,

$$\kappa^g := \mathcal{W}_{\mathbf{P}_g}(\tilde{\gamma}). \quad (33)$$

Then, the inverse problem (12) can be re-written as

$$\tilde{\gamma}^{\text{ng}} = \tilde{\mathbf{A}} \kappa^{\text{ng}} + \tilde{\mathbf{n}}, \quad (34)$$

where  $\tilde{\gamma}^{\text{ng}}$  denotes the residual shear map

$$\tilde{\gamma}^{\text{ng}} := \tilde{\gamma} - \tilde{\mathbf{A}} \kappa^g. \quad (35)$$

Then, PnPMass can be used to estimate  $\kappa^{\text{ng}}$ .

In order this approach to remain consistent with the previous theoretical framework, the denoiser must be trained on a suitable dataset. Specifically, we consider the training set  $(\kappa_{0,i}, \kappa_i)_{i=1}^n$  introduced in Sect. 3.2. Then, for each  $i \in \{0, \dots, n\}$ , we compute the Gaussian component  $\kappa_i^g$  from the noisy input  $\kappa_{0,i}$ , using a Wiener filter with power spectrum  $\mathbf{P}_g$ . Finally, we get the residual training set  $(\kappa_{0,i}^{\text{ng}}, \kappa_i^{\text{ng}})_{i=1}^n$  by subtracting  $\kappa_i^g$  to both the noisy input and the ground truth.

## 4. Uncertainty quantification

In Sect. 4.1, we introduce a fast UQ method for PnPMass. This approach is based on moment networks, originally proposed by Jeffrey & Wandelt (2020) to quantify uncertainty in end-to-end deep learning models such as DeepMass.

To the best of our knowledge, this is the first UQ method within the PnP framework that does not rely on ensembles or posterior sampling—both of which can be computationally demanding. Ensemble-based approaches estimate uncertainty by training and evaluating multiple networks, capturing variability across model parameters (Shi et al. 2021; Terris et al. 2025). Posterior sampling methods, in contrast, are Bayesian UQ methods that seek to approximate the posterior distribution of the reconstructed images, given some implicit or explicit priors. For example, Laumont et al. (2022) combined implicit PnP priors with Langevin diffusion to draw posterior samples. Alternatively, Ekmekci & Cetin (2021) proposed a Bayesian extension of the PnP framework by placing a prior over the denoiser’s parameters and propagating uncertainty through the reconstruction pipeline.

A sampling-free method was introduced by Postels et al. (2019) to approximate uncertainty in Monte-Carlo dropout networks. This approach could in principle be adapted to the Bayesian PnP framework proposed by Ekmekci & Cetin (2021) as a way to reduce computational costs. This line of research targets uncertainties in the model design and parameters—commonly referred to as epistemic uncertainty—and is left for future work. In contrast, the present study assumes perfect model design and training, and instead quantifies irreducible uncertainty arising from data noise—known as aleatoric uncertainty. We refer readers to Abdar et al. (2021) for a broader discussion of the distinction between epistemic and aleatoric uncertainty.

Next, in Sect. 4.2, we describe the CQR algorithm (Romano et al. 2019), which was adapted for mass mapping in a previous work (Leterme et al. 2025). This method serves as a postprocessing step that can be applied to any reconstruction method with an initial uncertainty estimate, providing per-pixel non-asymptotic marginal coverage guarantees without relying on prior assumptions about the data distribution.

### 4.1. Variance estimation with moment networks

In Sect. 4.1.1, we adapt the main principles of posterior variance estimation using moment networks, as described by Jeffrey & Wandelt (2020), to DeepMass specifically. Then, in Sect. 4.1.2, we extend this approach to the PnP framework and provide theoretical insights supporting its use. Finally, in Sect. 4.1.3, we explain how to get error bars from the estimated posterior variance.

#### 4.1.1. Moment networks for DeepMass

Given a simulated dataset  $(\tilde{\gamma}_i, \kappa_i)_{i=1}^n$ , where the pairs  $(\tilde{\gamma}_i, \kappa_i)$  are i.i.d. samples of the ground truth convergence maps and observed noisy shear maps, DeepMass attempts to solve the mass mapping problem by learning a deep neural network  $\mathcal{M}_w$  on  $(\tilde{\gamma}_i, \kappa_i)_{i=1}^n$  according to

$$\hat{w} \in \operatorname{argmin}_w \frac{1}{n} \sum_{i=1}^n \|\mathcal{M}_w(\tilde{\gamma}_i) - \kappa_i\|^2. \quad (36)$$

As  $n \rightarrow \infty$ , (36) is expected to approach a minimizer of the population risk, *i.e.*

$$\hat{w} \in \operatorname{argmin}_w \mathbb{E} \left[ \|\mathcal{M}_w(\tilde{\Gamma}) - \mathbf{K}\|^2 \right], \quad (37)$$

where the expectation is to be understood with respect to the joint distribution of  $(\mathbf{K}, \tilde{\Gamma})$ .

DeepMass adopts a Bayesian perspective and attempts to interpret (37) as the solution to

$$\min_{\mathcal{D} \text{ is } \mu_{\tilde{\Gamma}|\mathbf{K}}\text{-measurable}} \mathbb{E} \left[ \|\mathcal{D}(\tilde{\Gamma}) - \mathbf{K}\|^2 \right]. \quad (38)$$

where  $\mu_{\tilde{\Gamma}|\mathbf{K}}$  is the conditional distribution of  $\tilde{\Gamma}$  given  $\mathbf{K}$ . The closed-form solution to (38) is known as the posterior conditional mean estimator

$$\widehat{\mathcal{D}}(\tilde{\gamma}) = \mathbb{E}[\mathbf{K} | \tilde{\Gamma} = \tilde{\gamma}]. \quad (39)$$

The key assumption in DeepMass is that the following approximation holds:

$$\widehat{\mathcal{D}}(\tilde{\gamma}) \approx \mathcal{M}_{\hat{w}}(\tilde{\gamma}). \quad (40)$$

Intuitively, this can make sense if the architecture of the neural network  $\mathcal{M}_w$ , seen as a parametrized class of functions, is expressive enough, in such a way that the two optimization problems (37) and (38) are close.

This reasoning can be extended to estimate higher-order moments, including the posterior conditional variance per pixel:

$$\mathbb{V}[\mathbf{K} | \tilde{\Gamma} = \tilde{\gamma}] := \mathbb{E} \left[ \left( \mathbf{K} - \mathbb{E}[\mathbf{K} | \tilde{\Gamma} = \tilde{\gamma}] \right)^2 \mid \tilde{\Gamma} = \tilde{\gamma} \right], \quad (41)$$

which is known to be the solution to

$$\min_{\mathcal{V} \text{ is } \mu_{\tilde{\Gamma}|\mathbf{K}}\text{-measurable}} \mathbb{E} \left[ \left\| \mathcal{V}(\tilde{\Gamma}) - (\mathbf{K} - \widehat{\mathcal{D}}(\tilde{\Gamma})) \right\|^2 \right]. \quad (42)$$

To this end, we consider a new neural network model  $\mathcal{G}_\omega$  trained on a dataset  $(\tilde{\gamma}_i, \mathbf{v}_i)_{i=1}^n$  by solving

$$\hat{\omega} \in \operatorname{argmin}_\omega \frac{1}{n} \sum_{i=1}^n \|\mathcal{G}_\omega(\tilde{\gamma}_i) - \mathbf{v}_i\|^2, \quad (43)$$

where we have defined the target  $\mathbf{v}_i := (\kappa_i - \mathcal{M}_{\hat{w}}(\tilde{\gamma}_i))^2$ . Therefore, similarly to what we have argued for (37), (43) is an empirical version of

$$\hat{\omega} \in \operatorname{argmin}_\omega \mathbb{E} \left[ \left\| \mathcal{G}_\omega(\tilde{\Gamma}) - (\mathbf{K} - \mathcal{M}_{\hat{w}}(\tilde{\Gamma})) \right\|^2 \right], \quad (44)$$

Comparing (42) and (44), combining (40) and (41), and arguing as above, we can reasonably assume that

$$\mathbb{V}[\mathbf{K} | \tilde{\Gamma} = \tilde{\gamma}] \approx \mathcal{G}_{\hat{\omega}}(\tilde{\gamma}). \quad (45)$$

The corresponding model is referred to as an order-2 moment network.

#### 4.1.2. Adaptation to PnPMass

The moment network approach is not directly applicable to the PnP framework for several reasons. First, PnP, which is iterative, does not necessarily have a Bayesian interpretation, let alone a posterior conditional mean (see Sect. 3.3 and Appendix F). Recall also that we do not want to train any network on a dataset that depends on the noise covariance matrix  $\tilde{\Sigma}$ , for flexibility reasons. However, we will now describe how, within the setting presented in Sect. 3, the posterior conditional variance can be estimated with an order-2 moment network trained on zero-mean white Gaussian noise.

Let  $\mathcal{D}_\theta$  be the denoiser network that has been trained by solving (23) on a training dataset  $(\kappa_{0,i}, \kappa_i)_{i=1}^n$ , where we have denoted  $\kappa_{0,i} := \kappa_i + \mathbf{n}_{0,i}$ , with  $\mathbf{n}_{0,i}$  being sampled from  $\mathcal{N}(\mathbf{0}, \tau_i^2 \mathbf{I})$  conditionally on  $\tau_i$ —see (22) and (27). The noise standard deviations  $\tau_i$  are samples from the uniform distribution on an interval  $[\tau_{\min}, \tau_{\max}]$  containing the bounds in (28). As discussed in Sect. 3.5.2,  $\tau$  is also an input of the denoiser network.

We now consider the random vector

$$\mathbf{K}_0 := \mathbf{K} + \mathbf{N}_0, \quad (46)$$

where  $\mathbf{N}_0$  has been introduced in (22). In the context where we consider the step-size  $\tau$  to be an outcome of  $\mathsf{T} \sim \mathcal{U}([\tau_{\min}, \tau_{\max}])$ ,  $\mathbf{N}_0$  is now a mixture of zero-mean Gaussians with uniform mixing over  $\mathsf{T}$ . The noisy inputs  $\kappa_{0,i}$  from the training set are then assumed to be drawn i.i.d. from  $\mathbf{K}_0$ . With a similar reasoning as in Sect. 4.1.1, we can infer that, given  $\tau$  and a noisy input  $\kappa_0$ ,

$$\mathcal{D}_\theta(\kappa_0, \tau) \approx \mathbb{E}[\mathbf{K} \mid \mathbf{K}_0 = \kappa_0, \mathsf{T} = \tau]. \quad (47)$$

For the posterior conditional variance, we consider a model  $\mathcal{G}_\omega$  trained on  $(\kappa_{0,i}, \mathbf{v}_i)_{i=1}^n$ , with

$$\mathbf{v}_i := (\kappa_i - \mathcal{D}_\theta(\kappa_{0,i}, \tau_i))^2, \quad (48)$$

and we get, following again Sect. 4.1.1, that

$$\mathcal{G}_\omega(\kappa_0, \tau) = \mathbb{V}[\mathbf{K} \mid \mathbf{K}_0 = \kappa_0, \mathsf{T} = \tau]. \quad (49)$$

Now, we will argue that, after reaching a sufficient number of iterations, the outputs of  $\mathcal{D}_\theta$  and  $\mathcal{G}_\omega$  respectively approximate the posterior conditional mean and variance given a noisy observation  $\tilde{\mathbf{F}} = \tilde{\mathbf{y}}$ . To this end, let  $\hat{\kappa}_0 := \mathcal{F}_{\tilde{\mathbf{y}}}(\hat{\kappa}, \tau)$  denote the output of the forward step applied to the fixed point, satisfying (19). In Sect. 3.1, we have informally established conditions on the training noise to favor small residuals  $\hat{\mathbf{r}}$ . Therefore, we consider (20) as a reasonable approximation:

$$\hat{\kappa}_0 \approx \kappa + \mathbf{n}_0, \quad \text{with } \mathbf{n}_0 := \tau \tilde{\mathbf{B}} \tilde{\mathbf{n}} \in \mathbb{R}^{K^2}. \quad (50)$$

For a number of iterations  $N_{\text{it}} \geq 1$ , denote  $\mathcal{H}_{\tilde{\mathbf{y}}}^{N_{\text{it}}}(\cdot, \tau)$  the  $N_{\text{it}}$ -th composition of the PnPMass fixed point operator  $\mathcal{H}_{\tilde{\mathbf{y}}}^{N_{\text{it}}}(\cdot, \tau)$ . Clearly, the PnPMass iteration (17) also reads

$$\kappa^{(N_{\text{it}})} = \mathcal{H}_{\tilde{\mathbf{y}}}^{N_{\text{it}}}(\kappa^{(0)}, \tau). \quad (51)$$

Denote  $\mathcal{P}(\tilde{\mathbf{y}}, \tau) := \mathcal{F}_{\tilde{\mathbf{y}}}(\kappa^{(N_{\text{it}})}, \tau)$  the output of the  $(N_{\text{it}} + 1)$ -th forward step. For  $N_{\text{it}}$  large enough, we have from Proposition 1 that  $\kappa^{(N_{\text{it}})} \approx \hat{\kappa}$  which, combined with (19) and (20) yields

$$\mathcal{P}(\tilde{\mathbf{y}}, \tau) \approx \mathcal{F}_{\tilde{\mathbf{y}}}(\hat{\kappa}, \tau) = \hat{\kappa}_0 \approx \kappa + \mathbf{n}_0, \quad (52)$$

and therefore,

$$\mathcal{P}(\tilde{\mathbf{F}}, \mathsf{T}) \approx \mathbf{K}_0, \quad (53)$$

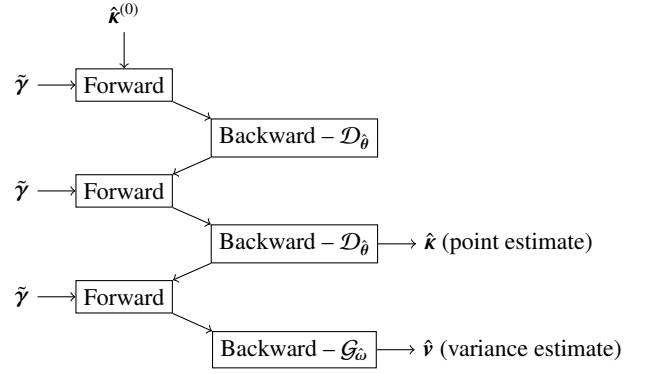


Fig. 1: Schematic representation of the PnPMass algorithm. Two iterations are shown for the point estimate (for illustration purposes only; more iterations are typically required in practice), followed by one additional iteration for the variance.

where  $\mathbf{K}_0$  has been introduced in (46). Plugging this into (47) and (49), replacing  $\kappa_0$  by  $\hat{\kappa}_0$ , we get, respectively:

$$\mathcal{D}_\theta(\hat{\kappa}_0, \tau) \approx \mathbb{E}[\mathbf{K} \mid \mathcal{P}(\tilde{\mathbf{F}}, \mathsf{T}) = \mathcal{P}(\tilde{\mathbf{y}}, \tau), \mathsf{T} = \tau] \quad (54)$$

and

$$\mathcal{G}_\omega(\hat{\kappa}_0, \tau) \approx \mathbb{V}[\mathbf{K} \mid \mathcal{P}(\tilde{\mathbf{F}}, \mathsf{T}) = \mathcal{P}(\tilde{\mathbf{y}}, \tau), \mathsf{T} = \tau]. \quad (55)$$

It is then sufficient that  $\mathcal{P}(\cdot, \tau)$  is injective to deduce that

$$\mathcal{D}_\theta(\hat{\kappa}_0, \tau) \approx \mathbb{E}[\mathbf{K} \mid \tilde{\mathbf{F}} = \tilde{\mathbf{y}}] \quad (56)$$

and

$$\mathcal{G}_\omega(\hat{\kappa}_0, \tau) \approx \mathbb{V}[\mathbf{K} \mid \tilde{\mathbf{F}} = \tilde{\mathbf{y}}]. \quad (57)$$

The overall algorithm implementing the PnPMass iteration is summarized in Fig. 1 and Algorithm 1.

#### 4.1.3. Uncalibrated pre-estimation of per-pixel error bars

Our goal is to provide per-pixel error bars with marginal and non-asymptotic coverage guarantees. More precisely, given a desired miscoverage rate  $\alpha \in ]0, 1[$ , we want to estimate  $\hat{\kappa}^-$  and  $\hat{\kappa}^+$  such that, for every  $k \in \{1, \dots, K^2\}$ ,

$$\mathbb{P}\{\mathbf{K}[k] \notin [\hat{\kappa}^-[k], \hat{\kappa}^+[k]] \mid \tilde{\mathbf{F}} = \tilde{\mathbf{y}}\} \leq \alpha. \quad (58)$$

To this end, we will start with a rough estimate based on a Gaussian assumption. This will then be calibrated (see Sect. 4.2). More precisely, we start with the following quantiles  $\hat{\kappa}^-$  and  $\hat{\kappa}^+$  from a Gaussian distribution of mean  $\hat{\kappa}$  and variance  $\hat{\mathbf{v}}$ , which are provided by Algorithm 1:

$$\hat{\kappa}^\pm[k] := \hat{\kappa}[k] \pm \Phi^{-1}\left(1 - \frac{\alpha}{2}\right) \hat{\sigma}[k], \quad (59)$$

where  $\Phi$  is the cumulative distribution function (CDF) of the normal distribution  $\mathcal{N}(0, 1)$ , and  $\hat{\sigma} = \sqrt{\hat{\mathbf{v}}}$  is the standard deviation estimate. If the conditional distribution of  $\mathbf{K}[k]$ , given  $\tilde{\mathbf{y}}$ , were  $\mathcal{N}(\hat{\kappa}[k], \hat{\mathbf{v}}[k])$ , then (58) would be satisfied by construction. This is however not the case, hence the need of a calibration step that we are about to describe.

---

**Algorithm 1** PnPMass with uncertainty quantification

---

**Require:** Noise covariance matrix  $\Sigma$ ;  
**Require:** Power spectrum  $\mathbf{P}_g$  (residual version only, Sect. 3.6);  
**Require:** Step-size  $\tau$  and number of iterations  $N_{it}$ ;  
**Require:** Denoiser  $\mathcal{D}_\theta$  trained on white Gaussian noise;  
**Require:** Order-2 moment network  $\mathcal{G}_\omega$ .

```
1: input: Noisy shear map  $\tilde{\gamma}$ .
2: if residual version then
3:   Compute Gaussian component:  $\kappa^g \leftarrow \mathcal{W}_{\mathbf{P}_g}(\tilde{\gamma})$ ;
4:   Update input (residual):  $\tilde{\gamma} \leftarrow \tilde{\gamma} - \tilde{\mathbf{A}}\kappa^g$ .
5: end if

6: initialize:  $\kappa^{(0)} = \mathbf{0}$ .
7: for  $i = 1, \dots, N_{it}$  do
8:   Forward step:  $\kappa_0^{(i)} \leftarrow \mathcal{F}_{\tilde{\gamma}}(\kappa^{(i-1)}, \tau)$ ;
9:   Backward step:  $\kappa^{(i)} \leftarrow \mathcal{D}_\theta(\kappa_0^{(i)}, \tau)$ .
10: end for
11: Set point estimate:  $\hat{\kappa} \leftarrow \kappa^{(N_{it})}$ .

12: Forward step:  $\hat{\kappa}_0 \leftarrow \mathcal{F}_{\tilde{\gamma}}(\hat{\kappa}, \tau)$ ;
13: Backward step (variance estimate):  $\hat{\nu} \leftarrow \mathcal{G}_\omega(\hat{\kappa}_0, \tau)$ .

14: if residual version then
15:   Update point estimate:  $\hat{\kappa} \leftarrow \hat{\kappa} + \kappa^g$ .
16: end if
17: return  $(\hat{\kappa}, \hat{\nu})$ .
```

---

## 4.2. Calibration with conformal predictions

In Sect. 4.1, the pre-estimates of the per-pixel error bars were based on several assumptions entailing several approximations:

- (47) and (49) state that the networks  $\mathcal{D}_\theta$  and  $\mathcal{G}_\omega$  are only approximations to the posterior mean and variance given  $\mathbf{K}_0 = \kappa_0$ , respectively. As discussed there, the approximation quality depends on factors such as the complexity of the neural networks used and the quality and diversity of the training data. As such, the method primarily captures aleatoric uncertainty—while epistemic uncertainty, associated with model expressiveness or limited knowledge, remains unaddressed.
- (52) is yet another approximation of the point estimate which, as we argued there, relies on the assumption that the fixed point  $\hat{\kappa}$  of PnPMass lies close enough to  $\kappa$ . In practice, this is not necessarily true and thus bias—non-zero residuals in (52)—may still be present. This is especially true near masked regions where the S/R is very low.
- The per-pixel error bars have been derived under a Gaussian assumption for the posterior distribution, making them only rough uncertainty estimates.

For all these reasons, the miscoverage inequality as stated in (58) is not guaranteed to hold. In this section, we present a calibration method directly inspired by CQR (Romano et al. 2019), for which we can obtain (marginal) coverage guarantees that are valid for finite samples (non-asymptotic) and do not depend on any assumption on the models or the data distribution (distribution-free). The choice of this method over other calibration approaches such as risk-controlling prediction sets (Angelopoulos et al. 2022), based on concentration inequalities, is motivated by the fact that it explicitly avoids overconservative error bands, making it suitable in a context where one wants to

get error bars as tight as possible. We refer readers to Leterme et al. (2025) for a detailed discussion on this topic.

In Sect. 4.2.1, we review the general principles of CQR for mass mapping, and we propose in Sect. 4.2.2 a method to minimize the size of the error bars without the need for model selection on a validation set.

### 4.2.1. General principles

We consider a calibration set  $(\tilde{\gamma}_i, \kappa_i)_{i=n+1}^{n+m}$  of size  $m \in \mathbb{N}$ . For each pair  $(\tilde{\gamma}_i, \kappa_i)$ , we compute the lower and upper bounds  $(\hat{\kappa}_i^-, \hat{\kappa}_i^+)$  from (59). Then, we compute a vector of conformity scores, denoted by  $\lambda_i \in \mathbb{R}^{K^2}$ , defined, for each pixel  $k \in \{1, \dots, K^2\}$ , by:

$$\lambda_i[k] = \max(\hat{\kappa}_i^-[k] - \kappa_i[k], \kappa_i[k] - \hat{\kappa}_i^+[k]). \quad (60)$$

Then, the calibration vector  $\lambda$  is obtained by computing, for each pixel, the  $(1 - \alpha)(1 + 1/m)$ -th empirical quantile of  $(\lambda_i[k])_{i=n+1}^{n+m}$ . The term  $(1 + 1/m)$ , which accounts for finite-sample correction, imposes a lower bound to the target error rate:  $\alpha \geq 1/(m + 1)$ . Finally, the calibrated bounds are defined as follows:

$$\hat{\kappa}_{\text{cqr}}^- := \hat{\kappa}^- - \lambda \quad \text{and} \quad \hat{\kappa}_{\text{cqr}}^+ := \hat{\kappa}^+ + \lambda. \quad (61)$$

We denote by  $\hat{\mathbf{K}}_{\text{cqr}}^-$  and  $\hat{\mathbf{K}}_{\text{cqr}}^+$  the random vectors from which  $\hat{\kappa}_{\text{cqr}}^-$  and  $\hat{\kappa}_{\text{cqr}}^+$  are drawn. Their random nature comes from that of  $\tilde{\mathbf{F}}$ , from which the noisy observation is drawn, as well as  $(\tilde{\mathbf{F}}_i, \mathbf{K}_i)_{i=n+1}^{n+m}$ , from which the calibration set is drawn. If  $(\tilde{\mathbf{F}}_i, \mathbf{K}_i)_{i=n+1}^{n+m} \cup \{(\tilde{\mathbf{F}}, \mathbf{K})\}$  are exchangeable (e.g., i.i.d.), and the conformity scores are almost surely distinct, then we have the following (marginal) miscoverage guarantee at pixel  $k$ :

$$\alpha - \frac{1}{m + 1} \leq \mathbb{P}\{\mathbf{K}[k] \notin [\hat{\mathbf{K}}_{\text{cqr}}^-[k], \hat{\mathbf{K}}_{\text{cqr}}^+[k]]\} \leq \alpha. \quad (62)$$

Observe that averaging over pixels, we deduce that the expected proportion of pixels whose mass estimates fall outside the corresponding predicted error interval also verifies the bounds in (62).

The bound in (62) presents a major difference compared to (58). Whereas the latter is conditional given  $\tilde{\gamma}$ , the former is marginalized over all possible outcomes of  $\tilde{\mathbf{F}}$ . Consequently, some inputs may lead to errors more likely than others. Conformal prediction with conditional guarantees is a very challenging problem and has only been solved in specific cases (Gibbs et al. 2025). We leave this for future work. In addition, the coverage guarantee provided in (62) is also marginalized over the distribution of all calibration sets. Therefore, accidentally picking an out-of-distribution calibration set may lead to a higher error rate than expected. This effect can be mitigated by increasing the size of the calibration set.

Note that the calibration procedure is not independent of the covariance matrix  $\Sigma$ , unlike the training phase. However, we point out that the former is several orders of magnitude cheaper than the latter, computationally speaking, as detailed in Sect. 6.4.

### 4.2.2. Minimizing the size of the error bars

We can easily show that the miscoverage guarantee from (62) still holds if the pre-calibration bounds  $\hat{\kappa}^\pm$ , introduced in (59), are replaced by

$$\hat{\kappa}_\mu^\pm[k] := \hat{\kappa}[k] \pm \mu \Phi^{-1}\left(1 - \frac{\alpha}{2}\right) \hat{\sigma}[k], \quad (63)$$

for any multiplicative constant  $\mu > 0$ . The calibration vector is then recomputed for each  $\mu$ , and is denoted by  $\lambda_\mu$ . This allows us to minimize the mean error bar size over  $\mu$ :

$$\mu^* \in \operatorname{argmin}_{\mu > 0} \mu \epsilon + \lambda_\mu \quad (64)$$

where  $\epsilon > 0$  denotes the mean half-size of the pre-calibration error bars (averaged over all test images and all pixels), and  $\lambda_\mu \in \mathbb{R}$  denotes the mean value of the calibration vector  $\lambda_\mu$ , which is a non-increasing function of  $\mu$ . This procedure is computationally inexpensive, since  $\hat{\kappa}_i$  and  $\hat{\sigma}_i$  are computed only once. For each candidate  $\mu$ , only the conformity scores  $\lambda_{\mu,i}$  and their corresponding quantiles must be recomputed in order to get  $\lambda_\mu$ .

## 5. Experimental settings

### 5.1. Datasets

In order to generate the training, validation, calibration and test sets, the ground truth convergence maps  $\kappa_i$  were obtained using the  $\kappa$ TNG dataset of mock convergence maps, as described below. The mass maps were generated from the full redshift distribution, following the same procedure as [Leterme et al. \(2025\)](#).

For the training and validation sets, the noisy inputs  $\kappa_{0,i}$  were obtained from  $\kappa_i$  by adding a white Gaussian noise with a standard deviation uniformly distributed between 0 and 0.2. The choice for this particular interval is explained in Sect. 5.2.1. At each training epoch, a new noise realization was drawn, with a newly picked noise level. For the calibration and test sets, the noisy shear maps  $\gamma_i$  were computed from  $\kappa_i$  using (7). The covariance matrix  $\Sigma$  was obtained by binning the weak lensing ‘‘S10’’ shear catalog created by [Schrabback et al. \(2010\)](#) (bright catalog only) at the  $\kappa$ TNG resolution (0.29 arcmin per pixel), and then applying (6). The intrinsic standard deviation  $\sigma_{\text{ell}}$  was estimated from the measured ellipticities and set to 0.39.

The S10 catalog is based on observations conducted by the NASA/ESA *Hubble* Space Telescope targeting the COSMOS field ([Scoville et al. 2007](#)) as well as photometric redshift measurements from [Mobasher et al. \(2007\)](#). It contains an average of 32 galaxies per square arcminute over a wide range of redshifts, which is consistent with what is expected from forthcoming surveys such as *Euclid*. This number excludes the galaxies with redshifts above 2.6 for the sake of consistency with the  $\kappa$ TNG dataset. It also ignores the masked pixels, without any observed galaxy. An example of mock convergence map  $\kappa_i$  from  $\kappa$ TNG, and the corresponding noisy shear map  $\gamma_i$ , is provided in Appendix H, Fig. H.1.

The  $\kappa$ TNG cosmological hydrodynamic simulations ([Osato et al. 2021](#)) include realizations of  $5 \times 5 \text{ deg}^2$  convergence maps for various source redshifts up to  $z = 2.6$ , at a 0.29 arcmin per pixel resolution, assuming a flat  $\Lambda$ CDM universe. Only one set of cosmological parameters was used to run the simulations:  $H_0 = 67.74 \text{ km} \cdot \text{s}^{-1} \cdot \text{Mpc}^{-1}$ ,  $\Omega_b = 0.0486$ ,  $\Omega_m = 0.3089$ ,  $n_s = 0.9667$ , and  $\sigma_8 = 0.8159$ . For training and validation, we respectively used 98 and 2 nearly independent realizations generated from a single lensing potential, that we randomly rotated and cropped to  $384 \times 384$  pixels, until we reached 70 560 images for training and 1 440 for validation. For calibration and testing respectively used 57 and 43 nearly independent realizations generated from another lensing potential. The test set was then obtained by extracting 512 non-overlapping<sup>1</sup> crops of size  $384 \times 384$  pixels, whereas the calibration set was obtained by

following the augmentation procedure described above, with a total of 1 024 images.

### 5.2. Other implementation details

#### 5.2.1. Parameters for PnPMass

With the specific value of  $\Sigma$  introduced in Sect. 5.1, the step-size  $\tau$  must be chosen in the interval  $]0, 0.176[$  to comply with (28). To get these bounds,  $\lambda_{\text{max}}$  and  $\lambda_{\text{min}}$  were computed using the power iteration method with 100 iterations—see Appendix E. To assess the sensitivity of PnPMass to the step-size, we tested several values of  $\tau$ , set to 50%, 75% and 100% of  $\tau_{\text{max}} := (1 + \rho)/\lambda_{\text{max}}$ , where  $\rho$  was taken arbitrarily close to 1.

According to (27), the denoiser must be able to operate on a noise level equal to the step-size  $\tau$ . For flexibility reasons, we have chosen to train the model on a realistic range of noise levels including the above interval, following the methodology described in Sect. 3.5.2. As detailed in Sect. 5.1, we used a uniform distribution between 0 and 0.2.

For the PnPMass variant on non-Gaussian residuals described in Sect. 3.6, the power spectrum  $\mathbf{P}_g$  was estimated on 2 048 ground-truth convergence maps from the training set. The Gaussian component  $\kappa^g$  was then computed using an iterative Wiener filtering method with 12 iterations and a step-size of  $1.61 \times 10^{-2}$ .

#### 5.2.2. Uncertainty quantification parameters

We selected a target error rate  $\alpha$  such that  $\Phi^{-1}(1 - \alpha/2) = 2$ , see (59). This setting, referred to as  $2\sigma$ -confidence, corresponds to  $\alpha \approx 4.55\%$ . We note that higher confidence levels require larger calibration sets due to the finite-sample correction: the CQR algorithm selects the  $(1 - \alpha)(1 + 1/m)$ -th empirical quantile of the conformity scores, which by definition must remain below 100%. Consequently, a  $2\sigma$ -confidence requires at least  $m = 21$  calibration samples, versus  $m = 370$  at  $3\sigma$  and  $m = 15\,787$  at  $4\sigma$ . In our experiments, we have chosen 1 024 calibration examples, which is way above the minimum requirement of 21 samples. With this setting, according to (62), the probability of miscoverage after calibration ranges between 4.45% and 4.55%.

#### 5.2.3. Denoiser training and PnPMass implementation

Our models are based on SUNet ([Fan et al. 2022](#)), a Swin Transformer-based architecture with 7.2 millions of trainable parameters, which we adapt to incorporate noise-level awareness. Following an approach similar to that used by ([Zhang et al. 2022](#)) for DRUNet, we introduce an additional input channel that encodes the noise standard deviation. Since our models are trained with stationary noise, this channel is filled with the constant value  $\sigma_i$  for each input  $\kappa_{0,i}$ .

We trained four models in total: two order-1 models  $\mathcal{D}_\theta$  for the point estimate, and two order-2 models  $\mathcal{G}_\omega$  for the variance (see Algorithm 1). In each case, we trained one model for standard PnPMass and another one for the variant on non-Gaussian residuals (see Sect. 3.6), using Adam as the optimizer and the squared  $\ell^2$  loss. Training was run for 100 epochs, with a batch size of 16. The learning rate was initialized at  $10^{-3}$  and reduced by a factor of 10 four times during training. For the PnPMass variant on non-Gaussian residuals, the Gaussian components  $\kappa_i^g$  were computed from  $\kappa_{0,i}$  using one-step Wiener filtering, which is feasible due to the noise being stationary, with the power spectrum  $\mathbf{P}_g$  introduced in Sect. 5.2.1.

<sup>1</sup> Accounting for the COSMOS boundaries.

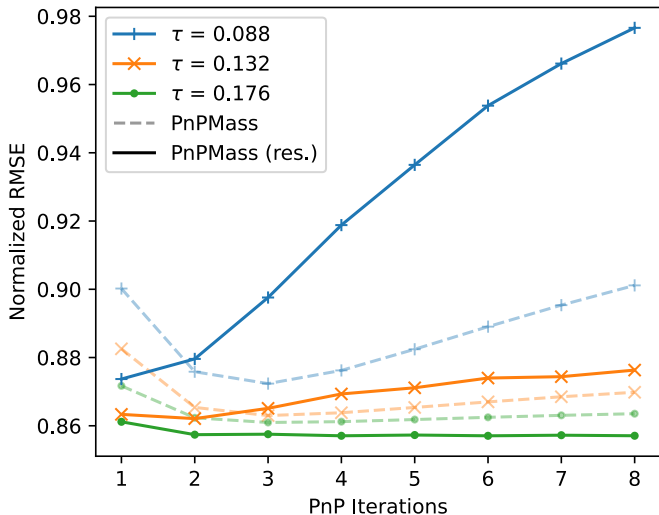


Fig. 2: Evolution of the mean RMSE along PnP iterations, computed on the  $\kappa$ TNG test set (512 images), for various step-sizes  $\tau$ . The results have been normalized w.r.t. to the  $\ell^2$ -norm of each image. We observe that the PnPMass variant on non-Gaussian residuals is more sensitive to the choice of  $\tau$ . In both cases, reconstruction accuracy increases with  $\tau$ .

In  $\mathcal{G}_0$ , the final mean-centering layer was replaced with a ReLU activation to enforce nonnegative outputs. To avoid vanishing gradients during training, however, the ReLU was only applied at inference time. The training set was built from the same dataset as the one used for training  $\mathcal{D}_\theta$ , with the ground truth derived from (48). Our PnPMass implementation is based on the DeepInverse library (Tachella et al. 2023),<sup>2</sup> with PyTorch backend.

## 6. Results and discussion

### 6.1. Reconstruction accuracy

#### 6.1.1. PnP iterations

We have run PnPMass for 8 iterations and plotted the evolution of the normalized root-mean-square error (RMSE) over the test set, restricted to active pixels, for various step-sizes  $\tau$ , for both standard PnPMass and its variant on non-Gaussian residuals. The results are shown in Fig. 2. Throughout the discussion, we refer to this metric as the reconstruction accuracy.

We observe that the RMSE decreases over the first iterations before either stabilizing or increasing again, depending on the step-size. Moreover, the reconstruction accuracy of PnPMass and its variant on non-Gaussian residuals increases as  $\tau$  increases in the devised range. PnPMass on non-Gaussian residuals is notably more sensitive to the choice of  $\tau$  than standard PnPMass. However, since the former incorporates prior knowledge of the Gaussian structure of the background mass distribution, it achieves the best reconstruction accuracy compared to the standard PnPMass at  $\tau = \tau_{\max}$ . Based on bootstrapping, the expected improvement after 8 iterations lies between  $6.04 \times 10^{-3}$  and  $6.88 \times 10^{-3}$  with 95% confidence.

From now on, we focus on the results obtained after 8 iterations, at  $\tau = \tau_{\max}$ . This choice was motivated by empirical obser-

Table 2: Reconstruction accuracy

Method	Normalized RMSE ( $\times 10^{-1}$ )
Wiener*	$8.86 \pm 0.34$
MCALens <sup>†</sup>	$8.74 \pm 0.44$
DeepMass <sup>‡</sup>	$8.53 \pm 0.48$
PnPMass	$8.64 \pm 0.50$
PnPMass (res.)	$8.58 \pm 0.49$

**Notes.** For each test example, the RMSE was computed over active pixels and normalized with respect to the  $\ell^2$ -norm of the ground-truth image. Then, the mean and standard deviation were evaluated across the test set (512 images). Although DeepMass slightly outperforms our methods, it lacks flexibility, as retraining is required for each new observation. \*Wiener was run for 12 iterations with a power spectrum estimated from 2048 ground-truth  $\kappa$ -maps in the training set. <sup>†</sup>MCALens was run for 16 iterations (early stopping), with a  $4.5\sigma$  detection threshold and a step-size of 0.088 for the non-Gaussian component. <sup>‡</sup>DeepMass was trained for 20 epochs on a UNet architecture with 280k parameters, following Jeffrey et al. (2020).

vations, as the reconstruction accuracy did not improve further beyond a few iterations.

#### 6.1.2. Benchmark against other approaches

We have compared the performance of the Wiener, MCALens, DeepMass and PnPMass algorithms in terms of reconstruction accuracy (RMSE on active pixels). The results are displayed in Table 2.

We find that our methods outperform the classical approaches (Wiener and MCALens), but fall slightly behind the reconstruction accuracy achieved by DeepMass. A likely explanation is that DeepMass has been finetuned for a specific mask  $\mathbf{M}$  and noise covariance  $\Sigma$ , whereas PnPMass is applicable across a wide range of configurations. However, as discussed in Sect. 2.2.2, this level of performance comes at the cost of re-training for each new observation, limiting its practicality. We therefore argue that PnPMass offers a very good trade-off between flexibility and reconstruction accuracy.

### 6.2. Uncertainty quantification results

For each mass mapping method introduced above and each example in the  $\kappa$ TNG test set, we computed the lower and upper bounds before and after calibration. Then, we measured the empirical miscoverage rate, that is, the percentage of active pixels falling outside the predicted bounds. For Wiener and MCALens, the error bars were simply initialized to 0 before calibration. Regarding DeepMass and PnPMass, the error bars before calibration were obtained using appropriate order-2 moment networks, as described in Sects. 4.1.1 and 4.1.2, respectively. We then applied calibration while minimizing the size of the error bars, as described in Sect. 4.2.2. The corresponding results, computed on the test set, are depicted in Figs. 3 and G.1 (Appendix G).

#### 6.2.1. Accuracy vs error bar size

After calibration, all methods achieve the same miscoverage rate, as guaranteed by (62), but the mean error bar size differs across methods.

First, let us compare our approach with Wiener and MCALens. PnPMass, in both standard and residual versions, produces smaller error bars than the two model-driven

<sup>2</sup> <https://deepinv.github.io/>

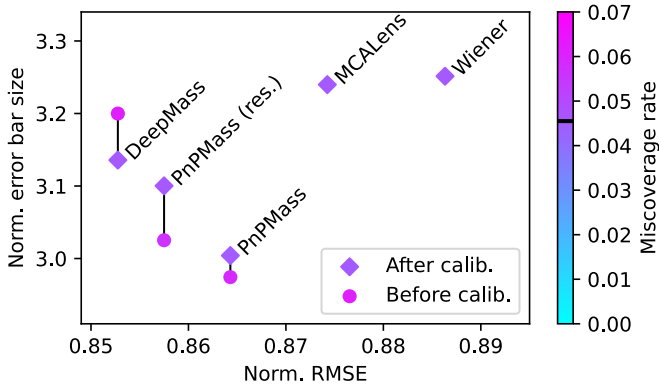


Fig. 3: Mean length of prediction intervals plotted against reconstruction accuracy, before and after calibration. Both metrics have been normalized w.r.t. to the  $\ell^2$ -norm of each image. The marker colors indicate empirical miscoverage rates, the target  $\alpha$  being marked on the color bar. The metrics are computed over the  $\kappa$ TNG test set (512 examples). All mass mapping algorithms were run with the same parameters as in Table 2. For Wiener and MCALens, only the post-calibration miscoverage rate is displayed, since their error bars were initialized to 0.

methods—see y-axis in Fig. 3. We hypothesize that the combination of higher reconstruction accuracy and adaptive pre-calibrated error bars obtained with order-2 moment networks helps discriminate between smooth regions and peak areas. This, in turn, may result in more refined uncertainty quantification by correctly assigning higher uncertainties near peaks. In contrast, Wiener and MCALens produce error bars that are independent of the input images: they are initialized at  $\mathbf{0}$  and subsequently calibrated using a parameter that depends only on pixel location.

More surprisingly, PnPMass also produces smaller error bars than DeepMass, despite being slightly less accurate. This result is statistically significant, as it is observed for all 512 test images. To explain this phenomenon, we propose the following conjecture: DeepMass detects more peaks than PnPMass, which improves reconstruction accuracy, but it also tends to hallucinate more peaks, which negatively affects the confidence level. In other words, the optimal precision-recall balance for peak detection depends on the metric one aims to prioritize. Consequently, a trade-off arises between reconstruction accuracy and error bar size. The same reasoning applies when comparing the standard and residual versions of PnPMass.

It is worth noting that error bars could, in principle, have been initialized at  $\mathbf{0}$  for all mass mapping methods, avoiding the need to train an order-2 moment network for DeepMass and PnPMass. However, this would ultimately result in larger calibrated error bars to compensate for the poorer initialization. A plot similar to Fig. 3, with zero-initialization for all methods, is shown in Appendix G, Fig. G.2.

### 6.2.2. Impact of calibration on the confidence intervals

For all methods based on moment networks, the pre-calibration error bars yield a miscoverage rate slightly above the target  $\alpha$ . Interestingly, calibration reduced the error bar size for DeepMass, which may seem counter-intuitive. This effect arises from the optimization strategy described in Sect. 4.2.2. Our interpretation is that, while error bars were under-estimated for most pixels, some regions—particularly around peaks—were overly conser-

Table 3: Computation times for  $\kappa$ TNG

Method	Training		Calibration	Inference
	Order 1	Order 2		
Wiener	–	–	9''	6''
MCALens	–	–	44''	24''
DeepMass <sup>‡</sup>	07:27'	46:33'	18''	7''
PnPMass	31:41'	47:20'	1'42''	50''
PnPMass (res.)	33:43'	43:44'	1'48''	54''

**Notes.** Training times were estimated for the first- and second-order moment networks on a single NVIDIA Quadro RTX 6000 GPU. Calibration and inference were performed on a single NVIDIA GeForce GTX 1080 Ti GPU, using 1 024 and 512 examples, respectively. Inference includes the computation of a point estimate, the initialization of error bars, and their calibration using the parameters computed at the previous stage. Note that the training times are expressed in hours, not minutes. <sup>‡</sup>The order-2 moment network for DeepMass was trained for 100 epochs, as the validation curve indicated that training was not yet complete after 20 epochs, in contrast with the order-1 network.

vative, leading to an overall overestimation that calibration was able to correct.

### 6.3. Mass mapping visualization

We applied both versions of PnPMass to the COSMOS shear field, that we have binned at the  $\kappa$ TNG resolution. A visual representation of both reconstructions is shown in Fig. 4, together with DeepMass and MMGAN reconstructions.<sup>3</sup> Additional visuals are provided in Appendix H, Fig. H.3, including the position of known x-ray clusters, as well as uncertainty maps (standard deviation per pixel).

A visual example of a reconstructed convergence map from a  $\kappa$ TNG simulation, along with its predicted standard deviation and bounds, is shown in Appendix H, Fig. H.2. While the post-calibration miscoverage rate remains constant on average, there are situations in which a given method may systematically fail to estimate uncertainty correctly. This is particularly noticeable for the Wiener solution around peak values—the blue spots in the bottom image indicate miscoverage. In contrast, our methods better account for peak values, as the order-2 moment networks tends to predict higher uncertainty in these regions. However, conformal prediction does not guarantee control of the miscoverage rate in specific situations such as peak values. One possible improvement would be to employ conditional conformal prediction (Gibbs et al. 2025), which we leave for future work.

### 6.4. Computation times

Computation times for training, calibration, and inference are reported in Table 3. While calibration and inference with PnPMass are slower than with DeepMass due to its iterative nature, these differences are negligible compared to training times, which are several orders of magnitude higher than inference times. This highlights one of the main advantages of our approach: unlike DeepMass and MMGAN, training is required only once.

## 7. Conclusion

In this work, we introduced PnPMass, a PnP-based mass mapping method that combines the strengths of DeepMass and

<sup>3</sup> We did not reproduce MMGAN ourselves; the reconstruction was downloaded from the Zenodo repository provided by the authors.

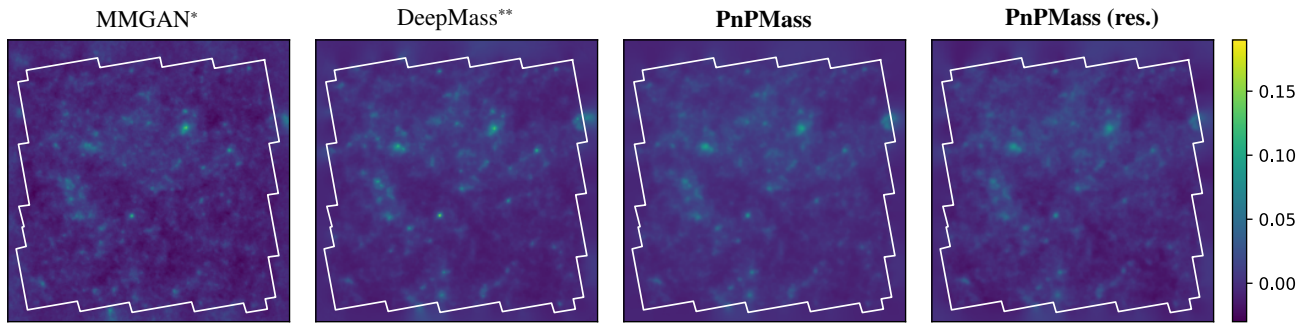


Fig. 4: Reconstruction of the COSMOS field with several deep-learning-based mass mapping methods. For consistency with MMGAN (left), we have concatenated the bright and faints catalogs before binning to the  $\kappa$ TNG resolution. \*Directly provided by Whitney et al. (2025). \*\*DeepMass was retrained to take into account the noise level and mask from the bright + faint catalogs.

DeepPosterior—namely, flexibility (no need to retrain for each new observation) and fast inference—while maintaining competitive reconstruction accuracy. We further proposed a fast UQ strategy for PnPMass based on moment networks, followed by conformal prediction to mitigate several sources of bias, including model uncertainty. Our results show that PnPMass yields the smallest calibrated error bars among all evaluated mass mapping methods. Together, these contributions make our approach well suited to handle the large data volumes expected from upcoming stage-IV surveys such as Euclid and Rubin.

Several directions remain open to fully integrate our framework into weak lensing pipelines. First, further investigations are needed to assess the robustness of our approach across different cosmologies. Our experiments focused on  $\kappa$ TNG, a dataset simulated from a single set of cosmological parameters. A more realistic setting would involve datasets spanning a range of cosmological models. Second, although conformal prediction provides coverage guarantees on average, it may fail to control miscoverage around peak structures, which are particularly important for cosmological parameter inference (Tersenov et al. 2025). A promising avenue to address this limitation is to employ conditional conformal prediction (Gibbs et al. 2025), rather than the standard version used here. Finally, it will be crucial to assess how uncertainties estimated at the mass-mapping stage propagate to cosmological parameter inference and affect the resulting FoM. In particular, this analysis could clarify whether the residual variant should be preferred over the standard version of PnPMass, as optimal cosmological parameter estimation may depend on a trade-off between reconstruction accuracy and size of the confidence intervals.

## Data availability

To ensure reproducibility, all software, scripts, and notebooks used in this study are available on GitHub.<sup>4</sup>

*Acknowledgements.* This work was funded by the TITAN ERA Chair project (contract no. 101086741) within the Horizon Europe Framework Program of the European Commission, and the French Agence Nationale de la Recherche (ANR-22-CE31-0014-01 TOSCA and ANR-18-CE31-0009 SPHERES).

## References

Abdar, M., Pourpanah, F., Hussain, S., et al. 2021, *Information Fusion*, 76, 243  
 Angelopoulos, A. N., Kohli, A. P., Bates, S., et al. 2022, in *Proceedings of the 39th International Conference on Machine Learning (PMLR)*, 717–730

<sup>4</sup> [https://github.com/hubert-leterme/weaklensing\\_uq.git](https://github.com/hubert-leterme/weaklensing_uq.git)

Aoyama, S. D., Osato, K., & Shirasaki, M. 2025, arXiv:2505.00345  
 Bobin, J., Starck, J.-L., Sureau, F., & Fadili, J. 2012, *Adv. Astron.*, 2012, e703217  
 Ebner, A. & Haltmeier, M. 2024, *IEEE Trans. Image Process.*, 33, 1476  
 Ekmekci, C. & Cetin, M. 2021, in *Proceedings of the IEEE/CVF International Conference on Computer Vision*, 4018–4027  
 Fan, C.-M., Liu, T.-J., & Liu, K.-H. 2022, in *2022 IEEE International Symposium on Circuits and Systems (ISCAS)*, 2333–2337  
 Finoguenov, A., Guzzo, L., Hasinger, G., et al. 2007, *The Astrophysical Journal Supplement Series*, 172, 182  
 Gibbs, I., Cherian, J. J., & Candès, E. J. 2025, *Journal of the Royal Statistical Society Series B: Statistical Methodology*, qkaf008  
 Hurault, S., Leclaire, A., & Papadakis, N. 2022, in *Proceedings of the 39th International Conference on Machine Learning (PMLR)*, 9483–9505  
 Jeffrey, N., Lanusse, F., Lahav, O., & Starck, J.-L. 2020, *MNRAS*, 492, 5023  
 Jeffrey, N. & Wandelt, B. D. 2020, in *Third Workshop on Machine Learning and the Physical Sciences (NeurIPS 2020)*  
 Kaiser, N. & Squires, G. 1993, *ApJ*, 404, 441  
 Kamilov, U. S., Bouman, C. A., Buzzard, G. T., & Wohlberg, B. 2023, *IEEE Signal Processing Magazine*, 40, 85  
 Kilbinger, M. 2015, *Rep. Prog. Phys.*, 78, 086901  
 Lanusse, F., Starck, J.-L., Leonard, A., & Pires, S. 2016, *A&A*, 591, A2  
 Laumont, R., Bortoli, V. D., Almans, A., et al. 2022, *SIAM J. Imaging Sci.*, 15, 701  
 Leterme, H., Fadili, J., & Starck, J.-L. 2025, *A&A*, 694, A267  
 Mobasher, B., Capak, P., Scoville, N. Z., et al. 2007, *The Astrophysical Journal Supplement Series*, 172, 117  
 Osato, K., Liu, J., & Haiman, Z. 2021, *MNRAS*, 502, 5593  
 Pesquet, J.-C., Repetti, A., Terris, M., & Wiaux, Y. 2021, *SIAM J. Imaging Sci.*, 14, 1206  
 Postels, J., Ferroni, F., Coskun, H., Navab, N., & Tombari, F. 2019, in *Proceedings of the IEEE/CVF International Conference on Computer Vision*, 2931–2940  
 Remy, B., Lanusse, F., Jeffrey, N., et al. 2023, *A&A*, 672, A51  
 Romano, Y., Patterson, E., & Candès, E. 2019, in *Advances in Neural Information Processing Systems*, Vol. 32 (Curran Associates, Inc.)  
 Ryu, E., Liu, J., Wang, S., et al. 2019, in *Proceedings of the 36th International Conference on Machine Learning (PMLR)*, 5546–5557  
 Schrabback, T., Hartlap, J., Joachimi, B., et al. 2010, *A&A*, 516, A63  
 Scoville, N., Abraham, R. G., Aussel, H., et al. 2007, *The Astrophysical Journal Supplement Series*, 172, 38  
 Shi, G., Zhu, Y., Tremblay, J., et al. 2021, in *2021 IEEE International Conference on Robotics and Automation (ICRA)*, 5200–5207  
 Shirasaki, M., Moriwaki, K., Oogi, T., et al. 2021, *MNRAS*, 504, 1825  
 Shirasaki, M., Yoshida, N., & Ikeda, S. 2019, *Phys. Rev. D*, 100, 043527  
 Starck, J.-L., Donoho, D. L., Fadili, M. J., & Rassat, A. 2013, *A&A*, 552, A133  
 Starck, J.-L., Murtagh, F., & Fadili, J. 2015, *Sparse Image and Signal Processing: Wavelets and Related Geometric Multiscale Analysis* (Cambridge University Press)  
 Starck, J.-L., Themelis, K. E., Jeffrey, N., Peel, A., & Lanusse, F. 2021, *A&A*, 649, A99  
 Tachella, J., Chen, D., Hurault, S., Terris, M., & Wang, A. 2023, *DeepInverse: A Deep Learning Framework for Inverse Problems in Imaging*  
 Terris, M., Repetti, A., Pesquet, J.-C., & Wiaux, Y. 2020, in *ICASSP 2020 - 2020 IEEE International Conference on Acoustics, Speech and Signal Processing (ICASSP)*, 8658–8662  
 Terris, M., Tang, C., Jackson, A., & Wiaux, Y. 2025, *MNRAS*, 537, 1608  
 Tersenov, A., Baumont, L., Starck, J.-L., & Kilbinger, M. 2025, *A&A*, 698, A25  
 Venkatakrisnan, S. V., Bouman, C. A., & Wohlberg, B. 2013, in *2013 IEEE Global Conference on Signal and Information Processing*, 945–948  
 Whitney, J. J., Liaudat, T. I., Price, M. A., Mars, M., & McEwen, J. D. 2025, *MNRAS*, 542, 2464  
 Zhang, K., Li, Y., Zuo, W., et al. 2022, *IEEE Transactions on Pattern Analysis and Machine Intelligence*, 44, 6360

## Appendix A: Proof of Proposition 1

We start with consider this preparatory lemma.

**Lemma 1.** *Suppose that (H.3) and (H.4) hold. Then, for  $\rho \in [\rho^*, 1]$ , the forward operator  $\mathcal{F}_{\tilde{\gamma}}(\cdot, \tau)$  is  $\rho$ -contractive on  $(\ker \tilde{\mathbf{B}}\tilde{\mathbf{A}})^\perp$  if, and only if, the step-size  $\tau$  satisfies (16). The smallest contraction factor  $\rho = \rho^*$  is obtained for  $\tau = \tau^*$ , with*

$$\tau^* := \frac{2}{\lambda_{\max} + \lambda_{\min}}. \quad (\text{A.1})$$

*Proof.* Denote for short the subspace  $\mathbb{V} := (\ker \tilde{\mathbf{B}}\tilde{\mathbf{A}})^\perp$ . By construction, and since (H.4) holds, we have:

$$\mathcal{F}_{\tilde{\gamma}}(\cdot, \tau) : \mathbb{V} \rightarrow \mathbb{V}. \quad (\text{A.2})$$

Let  $\boldsymbol{\kappa}'$  and  $\boldsymbol{\kappa}'' \in \mathbb{V}$ . The forward operator is an affine map, and we thus have

$$\mathcal{F}_{\tilde{\gamma}}(\boldsymbol{\kappa}', \tau) - \mathcal{F}_{\tilde{\gamma}}(\boldsymbol{\kappa}'', \tau) = (\mathbf{I} - \tau\tilde{\mathbf{B}}\tilde{\mathbf{A}})(\boldsymbol{\kappa}' - \boldsymbol{\kappa}''). \quad (\text{A.3})$$

Since  $\tilde{\mathbf{B}}\tilde{\mathbf{A}}$  is symmetric positive definite on the orthogonal to its kernel, the Lipschitz constant  $L_\tau$  of  $\mathcal{F}_{\tilde{\gamma}}(\cdot, \tau)$  on  $\mathbb{V}$  is exactly given by

$$L_\tau = \max(|1 - \tau\lambda_{\min}|, |1 - \tau\lambda_{\max}|). \quad (\text{A.4})$$

Consequently,  $\mathcal{F}_{\tilde{\gamma}}(\cdot, \tau)$  is  $\rho$ -contractive on  $\mathbb{V}$  if, and only if,  $L_\tau \leq \rho$ . Expanding this inequality, and considering that  $\lambda_{\min} \leq \lambda_{\max}$ , this is equivalent to (16). The lower bound  $\rho^*$  introduced in (15) ensures the non-emptiness of the interval. Moreover, setting  $\rho = \rho^*$  reduces the range of possible step-size values to  $\tau = \tau^*$  such as introduced in (A.1). Finally, having  $\rho < 1$  provides the contractive property of  $\mathcal{F}_{\tilde{\gamma}}(\cdot, \tau)$ .

Let us turn to the proof of Proposition 1.

*Proof.* According to (H.1) and (A.2), both  $\mathcal{D}_\theta$  and  $\mathcal{F}_{\tilde{\gamma}}(\cdot, \tau)$  map  $\mathbb{V}$  to  $\mathbb{V}$ . Combining this with the non-expansiveness of  $\mathcal{D}_\theta$  on  $\mathbb{V}$  (H.2), we have, for all  $\boldsymbol{\kappa}'$  and  $\boldsymbol{\kappa}'' \in \mathbb{V}$ ,

$$\|\mathcal{H}_{\tilde{\gamma}}(\boldsymbol{\kappa}', \tau) - \mathcal{H}_{\tilde{\gamma}}(\boldsymbol{\kappa}'', \tau)\| \leq \|\mathcal{F}_{\tilde{\gamma}}(\boldsymbol{\kappa}', \tau) - \mathcal{F}_{\tilde{\gamma}}(\boldsymbol{\kappa}'', \tau)\|. \quad (\text{A.5})$$

Invoking now Lemma 1 and using the step-size choice in (H.5), we get

$$\|\mathcal{H}_{\tilde{\gamma}}(\boldsymbol{\kappa}', \tau) - \mathcal{H}_{\tilde{\gamma}}(\boldsymbol{\kappa}'', \tau)\| \leq \rho \|\boldsymbol{\kappa}' - \boldsymbol{\kappa}''\|. \quad (\text{A.6})$$

Clearly,  $\mathcal{H}_{\tilde{\gamma}}(\cdot, \tau)$  is a  $\rho$ -contraction on  $\mathbb{V}$ . Since  $\mathbb{V}$  is obviously a complete metric space, we can now invoke the Banach-Picard fixed point theorem on  $\mathcal{H}_{\tilde{\gamma}}(\cdot, \tau)$  to get that it has a unique fixed point  $\hat{\boldsymbol{\kappa}} \in \mathbb{V}$ . Moreover, using (H.1) and an induction argument,  $(\boldsymbol{\kappa}^{(k)})_{k \in \mathbb{N}} \subset \mathbb{V}$ , and thus, the sequence converges linearly to  $\hat{\boldsymbol{\kappa}}$  at the rate  $\rho$ .

## Appendix B: Insights into convergence properties

In this section, we sketch a mathematical framework for studying the convergence properties of our algorithm, which leads to constrain the noise level at which the denoiser must be trained, as explained in Sect. 3.2.

Inserting (12) into the fixed-point equation (18), we infer that

$$\hat{\boldsymbol{\kappa}} = \mathcal{D}_\theta(\boldsymbol{\kappa} + \hat{\boldsymbol{r}} + \tau\tilde{\mathbf{B}}(-\tilde{\mathbf{A}}\hat{\boldsymbol{r}} + \tilde{\boldsymbol{n}})) = \mathcal{D}_\theta(\boldsymbol{\kappa} + (\mathbf{I} - \tau\tilde{\mathbf{B}}\tilde{\mathbf{A}})\hat{\boldsymbol{r}} + \boldsymbol{n}_0), \quad (\text{B.1})$$

where we denoted the residual  $\hat{\boldsymbol{r}} := \hat{\boldsymbol{\kappa}} - \boldsymbol{\kappa}$  and  $\boldsymbol{n}_0 = \tau\tilde{\mathbf{B}}\tilde{\boldsymbol{n}}$ . Observe that  $\boldsymbol{n}_0$  is a sample of  $\mathbf{N}_0$  as defined in (22).

Clearly,  $\mathcal{D}_\theta$  acts as a denoiser on the true convergence map  $\boldsymbol{\kappa}$  corrupted by the ‘‘noise’’  $(\mathbf{I} - \tau\tilde{\mathbf{B}}\tilde{\mathbf{A}})\hat{\boldsymbol{r}} + \boldsymbol{n}_0$ . Intuitively, one would like  $(\mathbf{I} - \tau\tilde{\mathbf{B}}\tilde{\mathbf{A}})\hat{\boldsymbol{r}}$  to be small enough so that the dominating part of the noise would be that from  $\boldsymbol{n}_0$ . This intuition is exact when  $\tilde{\mathbf{A}} = \mathbf{I}$  (i.e. denoising), in which case, with the natural choice  $\tilde{\mathbf{B}} = \mathbf{I}$  and  $\tau = 1$ , (B.1) reads  $\hat{\boldsymbol{\kappa}} = \mathcal{D}_\theta(\boldsymbol{\kappa} + \boldsymbol{n}_0)$  with  $\boldsymbol{n}_0 = \tilde{\boldsymbol{n}}$ . One should then train the denoiser with noise  $\boldsymbol{n}_0$ .

To get some insight into this intuition in the general case, let us now bound the residual  $\hat{\boldsymbol{r}}$ . Let  $\boldsymbol{\zeta}$  be a sample of the zero-mean random noise  $\mathbf{Z}$  used during training, and assume that the support of the distribution of  $\mathbf{K} + \mathbf{Z}$  is contained in  $(\ker \tilde{\mathbf{B}}\tilde{\mathbf{A}})^\perp$ . Subtracting  $\boldsymbol{\kappa}$  to both sides of (B.1), we have:

$$\|\hat{\boldsymbol{r}}\| \leq \left\| \mathcal{D}_\theta(\boldsymbol{\kappa} + (\mathbf{I} - \tau\tilde{\mathbf{B}}\tilde{\mathbf{A}})\hat{\boldsymbol{r}} + \boldsymbol{n}_0) - \mathcal{D}_\theta(\boldsymbol{\kappa} + \boldsymbol{\zeta}) \right\| + \left\| \mathcal{D}_\theta(\boldsymbol{\kappa} + \boldsymbol{\zeta}) - \boldsymbol{\kappa} \right\| \\ \leq \left\| (\mathbf{I} - \tau\tilde{\mathbf{B}}\tilde{\mathbf{A}})\hat{\boldsymbol{r}} + \boldsymbol{n}_0 - \boldsymbol{\zeta} \right\| + \left\| \mathcal{D}_\theta(\boldsymbol{\kappa} + \boldsymbol{\zeta}) - \boldsymbol{\kappa} \right\| \quad (\text{B.2})$$

$$\leq \rho \|\hat{\boldsymbol{r}}\| + \|\boldsymbol{n}_0 - \boldsymbol{\zeta}\| + \left\| \mathcal{D}_\theta(\boldsymbol{\kappa} + \boldsymbol{\zeta}) - \boldsymbol{\kappa} \right\|, \quad (\text{B.3})$$

where we used (H.2) in (B.2), and the triangle inequality and Lemma 1 (Appendix A) in (B.3). We then deduce, after taking the expectation with respect to the joint distribution of  $(\mathbf{K}, \mathbf{N}, \mathbf{Z})$ , that

$$\mathbb{E} \left[ \|\hat{\boldsymbol{r}}\| \right] \leq (1 - \rho)^{-1} \left( \mathbb{E} \left[ \|\mathbf{N}_0 - \mathbf{Z}\| \right] + \mathbb{E} \left[ \|\mathcal{D}_\theta(\mathbf{K} + \mathbf{Z}) - \mathbf{K}\| \right] \right) \\ \leq (1 - \rho)^{-1} \left( \mathbb{E} \left[ \|\mathbf{N}_0 - \mathbf{Z}\|^2 \right]^{\frac{1}{2}} + \mathbb{E} \left[ \|\mathcal{D}_\theta(\mathbf{K} + \mathbf{Z}) - \mathbf{K}\|^2 \right]^{\frac{1}{2}} \right), \quad (\text{B.4})$$

where we used Jensen’s inequality.

We aim to minimize the expected norm of the residual such as introduced above. Ideally, the denoiser  $\mathcal{D}_\theta$  would be trained to minimize the population quadratic risk, which is nothing but the second term in the upper bound (B.4). In practice, however, training is performed using the empirical quadratic risk, which introduces an additional generalization error term that must be accounted for. Regarding the first term in (B.4), it captures the discrepancy between the noise in training and that in the PnP iteration. We have

$$\mathbb{E} \left[ \|\mathbf{N}_0 - \mathbf{Z}\|^2 \right] = \mathbb{E} \left[ \|\mathbf{N}_0\|^2 \right] + \mathbb{E} \left[ \|\mathbf{Z}\|^2 \right] - 2\nu \mathbb{E} \left[ \|\mathbf{N}_0\|^2 \right]^{1/2} \mathbb{E} \left[ \|\mathbf{Z}\|^2 \right]^{1/2},$$

where  $\nu \in [-1, 1]$  is the correlation coefficient between  $\mathbf{N}_0$  and  $\mathbf{Z}$ . Minimizing the above expression wrt  $\mathbb{E} \left[ \|\mathbf{Z}\|^2 \right]$  and  $\nu$  gives that the optimal values are, respectively,  $\mathbb{E} \left[ \|\mathbf{N}_0\|^2 \right]$  and 1. Clearly, the noise  $\mathbf{Z}$  ought to have the same variance as  $\mathbf{N}_0$  and has correlation 1 with it.

## Appendix C: Properties of $\tilde{\mathbf{B}}\tilde{\mathbf{A}}$

Recall that  $\tilde{\mathbf{B}}\tilde{\mathbf{A}} := \tilde{\mathbf{A}}^\top \tilde{\boldsymbol{\Sigma}}^{-1/2} \tilde{\mathbf{A}}$  with the choice made in (24). This is obviously a symmetric positive semidefinite matrix, hence (H.3) follows. Observe also that:

$$\text{ran } \tilde{\mathbf{B}} = \text{ran } \tilde{\mathbf{A}}^\top \tilde{\boldsymbol{\Sigma}}^{-1/2} = \text{ran } \tilde{\mathbf{A}}^\top, \quad (\text{C.1})$$

since  $\tilde{\boldsymbol{\Sigma}}$  is invertible. On the other hand,

$$(\ker \tilde{\mathbf{B}}\tilde{\mathbf{A}})^\perp = (\ker \tilde{\mathbf{A}}^\top \tilde{\boldsymbol{\Sigma}}^{-1/2} \tilde{\mathbf{A}})^\perp = (\ker \tilde{\mathbf{A}}^\top \tilde{\mathbf{A}})^\perp = (\ker \tilde{\mathbf{A}})^\perp, \quad (\text{C.2})$$

since  $\tilde{\boldsymbol{\Sigma}}$  is invertible. As  $\text{ran } \tilde{\mathbf{A}}^\top = (\ker \tilde{\mathbf{A}})^\perp$ , we conclude that (H.4) holds.

## Appendix D: Proof of (26)

We embark from (11) to see that

$$\mathbf{A}^\top \mathbf{A} = \text{Re}(\mathbf{A}^* \mathbf{A}),$$

where  $\mathbf{A}^*$  is the adjoint matrix of  $\mathbf{A}$ . Using now (2), we get

$$\mathbf{A}^* \mathbf{A} = \mathbf{F}^* |\mathbf{P}|^2 \mathbf{F}.$$

From (3), it follows that  $|\mathbf{P}|^2$  is a diagonal matrix with

$$|\mathbf{P}[0, 0]| = 0 \quad \text{and} \quad |\mathbf{P}[i, i]| = 1, \forall i \geq 1.$$

This entails that

$$\mathbf{A}^* \mathbf{A} = \mathbf{F}^* \mathbf{F} - \mathbf{F}[1, :]^\top \mathbf{F}[1, :],$$

where  $\mathbf{F}[1, :]$  is the first row of  $\mathbf{F}$ . Let  $\mathbb{1}$  be the column vector of ones of size  $K^2$ . Since  $\mathbf{F}[1, :] := \mathbb{1}^\top / K$  (the zero frequency component), and  $\mathbf{F}$  is unitary, we get that

$$\mathbf{A}^* \mathbf{A} = \mathbf{I} - \mathbb{1} \mathbb{1}^\top / K^2 = \mathbf{I} - 1/K^2.$$

## Appendix E: Computing $\lambda_{\max}$ and $\lambda_{\min}$

$\lambda_{\max}$  can be easily computed from the power iteration applied to  $\tilde{\mathbf{A}}^\top \tilde{\Sigma}^{-1/2} \tilde{\mathbf{A}}$  starting from a random uniform vector. We now turn to computing the smallest non-zero eigenvalue of  $\tilde{\mathbf{A}}^\top \tilde{\Sigma}^{-1/2} \tilde{\mathbf{A}}$ . From Appendix C, we have  $\tilde{\mathbf{A}}^\top \tilde{\Sigma}^{-1/2} \tilde{\mathbf{A}} = \ker \mathbf{A} = \text{ran } \mathbb{1}$ , whose orthogonal is the subspace of zero-mean vectors. Let  $\lambda_1 = 0 < \lambda_2 = \lambda_{\min} \leq \dots \leq \lambda_{K^2} = \lambda_{\max}$ , be the eigenvalues of  $\tilde{\mathbf{A}}^\top \tilde{\Sigma}^{-1/2} \tilde{\mathbf{A}}$  sorted in ascending order. Denote  $\mathbf{u}_i$  the corresponding unit norm eigenvectors, where  $\mathbf{u}_1 = \mathbb{1}^\top / K$ . Define the matrix  $\mathbf{C} := \lambda_{\max} \mathbf{I} - \tilde{\mathbf{A}}^\top \tilde{\Sigma}^{-1/2} \tilde{\mathbf{A}}$ , whose eigenvalues are  $\lambda_{\max} - \lambda_i$ , and eigenvectors are  $\mathbf{u}_i$ . The key observation is that  $\mathbf{C}$  is again symmetric positive semidefinite and, orthogonally to  $\text{ran } \mathbb{1}$ , the largest eigenvalue of  $\mathbf{C}$  is  $\lambda_{\max} - \lambda_{\min}$ .

The idea now is to apply the power iteration to  $\mathbf{C}$  with an appropriate initial vector. For instance, we draw a vector  $\mathbf{x}_0$  from the uniform distribution (or any distribution which has a density with respect to the Lebesgue measure), in which case we can write

$$\mathbf{x}_0 = \sum_{i=1}^{K^2} c_i \mathbf{u}_i,$$

where, for all  $i$ ,  $c_i \neq 0$  with probability one. We then project  $\mathbf{x}_0$  on  $(\ker \mathbf{A})^\perp = (\text{ran } \mathbb{1})^\perp$ , *i.e.*,

$$\bar{\mathbf{x}}_0 = \mathbf{x}_0 - \frac{1}{K^2} \sum_{i=1}^{K^2} \mathbf{x}_0[i] \mathbf{u}_i.$$

Since  $(\ker \mathbf{A})^\perp$  is the span of  $(\mathbf{u}_i)_{i \geq 2}$ , we have

$$\bar{\mathbf{x}}_0 = \sum_{i=2}^{K^2} c_i \mathbf{u}_i.$$

Hence

$$\mathbf{C}^k \bar{\mathbf{x}}_0 = c_2 (\lambda_{\max} - \lambda_{\min})^k \mathbf{u}_2 + \sum_{i=3}^{K^2-1} c_i (\lambda_{\max} - \lambda_i)^k \mathbf{u}_i.$$

Applying the power iteration to  $\mathbf{C}$  with initial vector  $\bar{\mathbf{x}}_0$  allows to compute  $\lambda_{\max} - \lambda_{\min}$ . Plugging the value of  $\lambda_{\max}$  (computed using, *e.g.*, power iteration) gives an estimate of  $\lambda_{\min}$ .

## Appendix F: PnP-Mass and the FBS algorithm

We assume the existence of a proper convex, lower semicontinuous function  $g$  such that

$$\mathcal{D}_{\hat{\theta}}(\boldsymbol{\kappa}', \tau) = \text{prox}_{\tau g}(\boldsymbol{\kappa}'), \quad (\text{F.1})$$

where the proximal operator is defined as

$$\text{prox}_{\tau g} : \boldsymbol{\kappa}' \mapsto \underset{\boldsymbol{\kappa}''}{\text{argmin}} \frac{1}{2} \|\boldsymbol{\kappa}'' - \boldsymbol{\kappa}'\|_2^2 + \tau g(\boldsymbol{\kappa}''). \quad (\text{F.2})$$

Under this assumption, the fixed-point iteration (31) can be written as

$$\mathcal{H}_{\tilde{\gamma}}(\boldsymbol{\kappa}', \tau) := \text{prox}_{\tau g} \left[ \boldsymbol{\kappa}' - \tau \nabla f_{\tilde{\gamma}}(\tilde{\mathbf{A}} \cdot)(\boldsymbol{\kappa}') \right], \quad (\text{F.3})$$

where we have considered the following data fidelity term

$$f_{\tilde{\gamma}}(\tilde{\mathbf{A}} \boldsymbol{\kappa}') := \frac{1}{2} \|\tilde{\gamma} - \tilde{\mathbf{A}} \boldsymbol{\kappa}'\|_{\tilde{\Sigma}^{-1/2}}^2. \quad (\text{F.4})$$

The operator (F.3) is nothing but the fixed-point operator of the well-known FBS algorithm. It consists of a forward step—gradient descent with respect to the data fidelity term  $f_{\tilde{\gamma}}(\tilde{\mathbf{A}} \cdot)$ —and a backward step—proximal mapping with respect to the regularization term  $g$ . This is the reason why PnP-type algorithms with an FBS structure are usually referred to as PnP-FBS in the literature (Ryu et al. 2019; Ebner & Haltmeier 2024).

It is well-known that if the step-size satisfies  $0 < \tau < 2 / \|\tilde{\mathbf{A}}^\top \tilde{\Sigma}^{-1/2} \tilde{\mathbf{A}}\|$ , then the sequence of iterates of FBS with operator (F.3) converges to a minimizer  $\hat{\boldsymbol{\kappa}}$  of the following minimization problem—similar in form to (8):

$$\hat{\boldsymbol{\kappa}} \in \underset{\boldsymbol{\kappa}'}{\text{argmin}} f_{\tilde{\gamma}}(\tilde{\mathbf{A}} \boldsymbol{\kappa}') + g(\boldsymbol{\kappa}'), \quad (\text{F.5})$$

with the proviso that the set of minimizers is non-empty.

The FBS has been widely used for astronomical data analysis; see the comprehensive treatment in (Starck et al. 2015). The iterative Wiener filtering algorithm (Bobin et al. 2012) for mass mapping (see Sect. 2.2.1), is also an instance of the FBS algorithm.

While some proximal operators can be seen as denoisers, the converse is clearly not true. Thus, there is no reason that a deep-learning based denoiser  $\mathcal{D}_{\hat{\theta}}(\cdot, \tau)$  to be interpreted as a proximal operator. At best, the denoiser network can be constrained during training to be firmly non-expansive, *i.e.* to be the resolvent of a maximally monotone set-valued operator as proposed in (Terzis et al. 2020). While this point of view brings interpretability, it is however not clear it leads to better denoising results. Consequently, PnP algorithms such as PnP-Mass are not expected to solve any optimization problem in general, hence the fixed-point perspective that we advocated in this paper.

It is worth recalling again (see Sect. 3.3) that the data fidelity term defined in (F.4) does not correspond to the negative log-likelihood typically used in Bayesian frameworks: the Mahalanobis norm would be defined with respect to  $\tilde{\Sigma}^{-1}$  rather than  $\tilde{\Sigma}^{-1/2}$ . Furthermore, the regularization function  $g$  does not necessarily correspond to a negative log-prior; see Starck et al. (2013) for a thorough discussion. As a result,  $\hat{\boldsymbol{\kappa}}$  should not be interpreted as a maximum a posteriori (MAP) estimate, even if (F.1) is satisfied.

## Appendix G: Additional plots

### G.1. Miscoverage rates before and after calibration

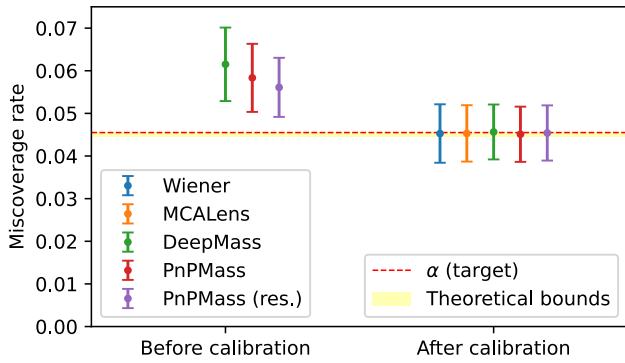


Fig. G.1: Empirical miscoverage rate over active pixels, before and after calibration (using 1 024 calibration examples). Error bars indicate the mean and standard deviation across the 512 test examples from the  $\kappa$ TNG dataset. As in Fig. 3, Wiener and MCALens results are only displayed after calibration. The theoretical bounds (in yellow) come from (62).

### G.2. Zero-initialization error bars

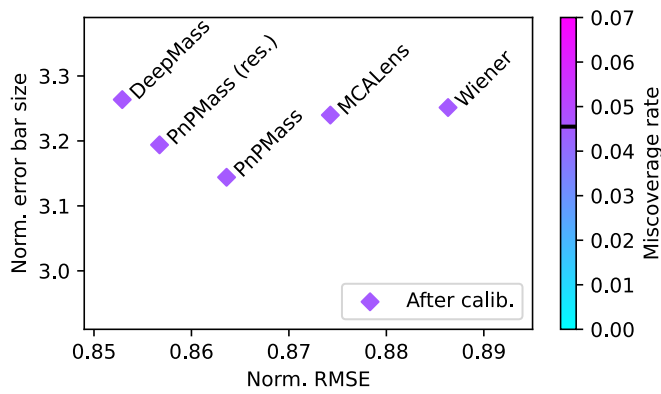


Fig. G.2: Mean length of prediction intervals plotted against reconstruction accuracy, after calibration. Unlike Fig. 3, all methods have been initialized with zero-valued error bars (no order-2 moment network).

We observe that ignoring the pre-calibration step with order-2 moment networks result in larger error bars for PnPMass and DeepMass, by comparison with Fig. 3. Furthermore, DeepMass now produces larger error bars than Wiener or MCALens, despite being significantly more accurate.

## Appendix H: Visual representations

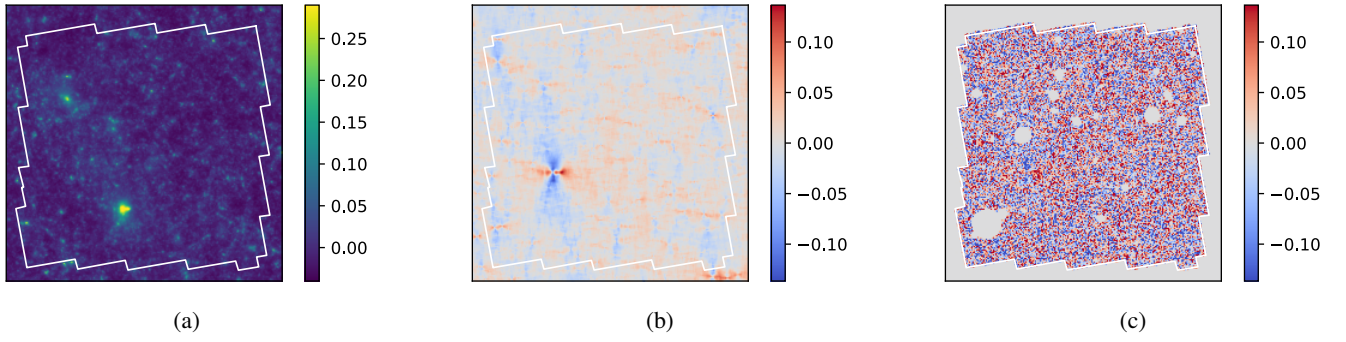


Fig. H.1: Example of mock convergence map obtained from  $\kappa$ TNG simulations (a), and the real part of the corresponding clean (b) and noisy (c) shear map. The COSMOS boundaries are delimited in white.

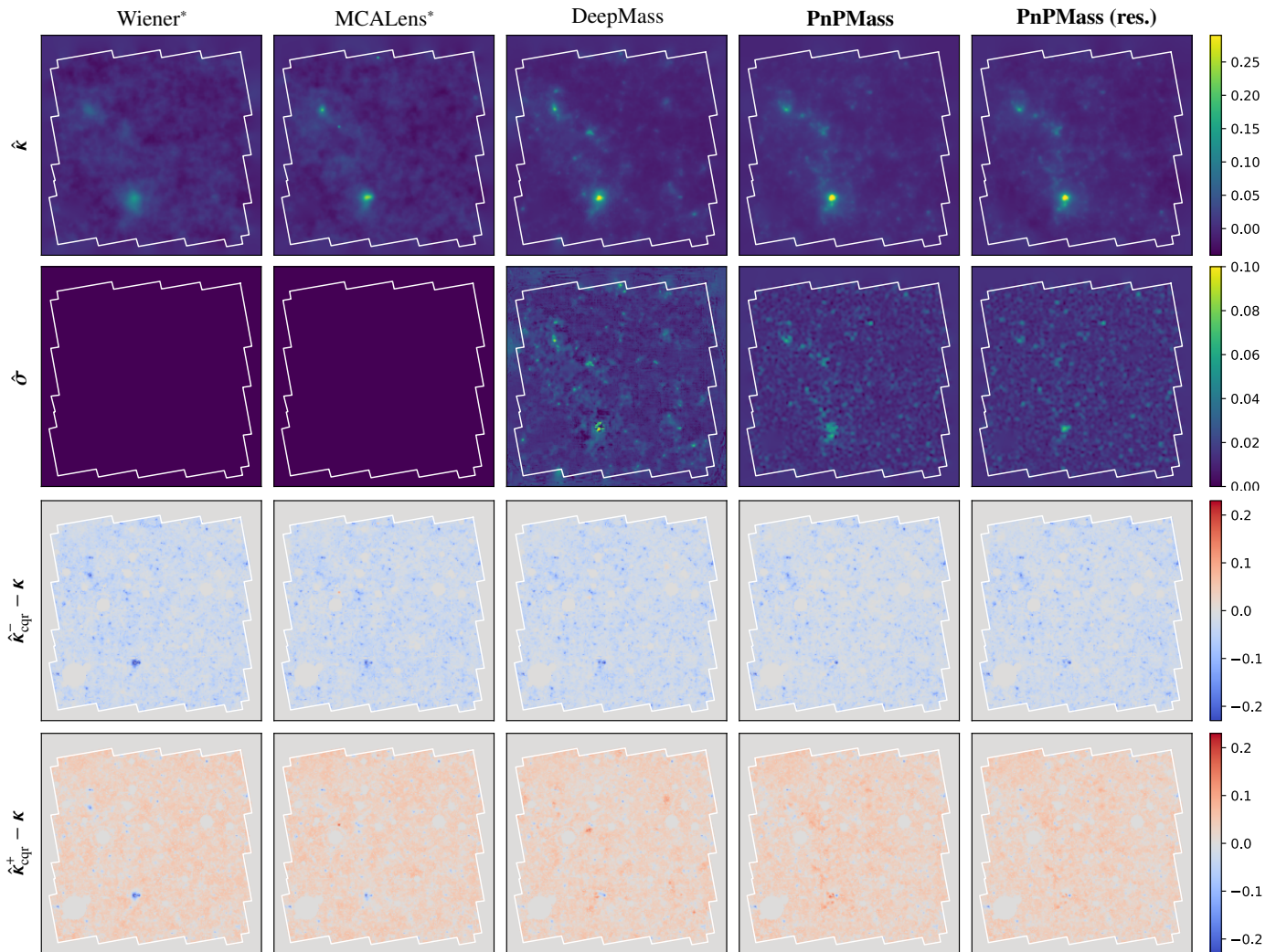


Fig. H.2: Example of mass mapping reconstructions on the  $\kappa$ TNG test dataset, for each mass mapping method, run with the same parameters as in Table 2. The corresponding ground truth convergence map  $\kappa$  and noisy input  $\gamma$  are displayed in Fig. H.1. Top row: Point estimates,  $\hat{\kappa}$ . Second row: Standard deviation estimates,  $\hat{\sigma}$ , obtained with order-2 moment networks (used for pre-calibration error bars). Bottom rows: Lower and upper bounds,  $\hat{\kappa}_{\text{cqr}}^-$  and  $\hat{\kappa}_{\text{cqr}}^+$ , after calibration with CQR. For visualization purpose, the bounds have been centered with respect to the ground truth  $\kappa$ . \*Zero-sized error bars before calibration.

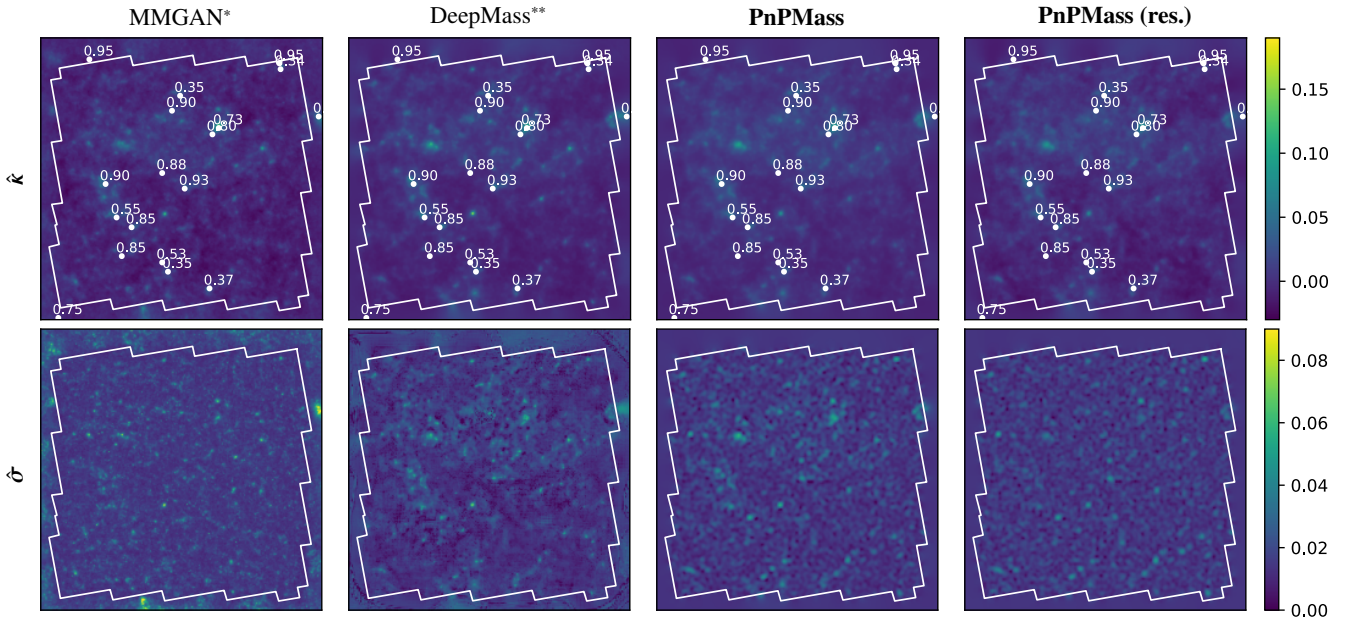


Fig. H.3: Reconstruction of the COSMOS field with several deep-learning-based mass mapping methods. For consistency with MMGAN (left), we have concatenated the bright and faints catalogs before binning to the  $\kappa$ TNG resolution. Top row: point estimates; the white scatter plot indicates the location of known x-ray clusters (Finoguenov et al. 2007). Bottom row: uncertainty maps, obtained with order-2 moment networks for PnPMass and DeepMass, and by computing the per-pixel standard deviation over 32 samples for MMGAN. \*Directly provided by Whitney et al. (2025). \*\*DeepMass was retrained to take into account the noise level and mask from the bright + faint catalogs.